arXiv:0709.0983v1 [astro-ph] 7 Sep 2007

THE LUMINOSITY FUNCTION OF LOW-REDSHIFT ABELL GALAXY CLUSTERS

Wayne A. Barkhouse,[1,2,4] H.K.C. Yee,[2,4] and Omar López-Cruz[3,4]
Accepted for publication in ApJ

ABSTRACT

We present the results from a survey of 57 low-redshift Abell galaxy clusters to study the radial dependence of the luminosity function (LF). The dynamical radius of each cluster, r_{200}, was estimated from the photometric measurement of cluster richness, B_{gc}. The shape of the LFs are found to correlate with radius such that the faint-end slope, α, is generally steeper on the cluster outskirts. The sum of two Schechter functions provides a more adequate fit to the composite LFs than a single Schechter function. LFs based on the selection of red and blue galaxies are bimodal in appearance. The red LFs are generally flat for $-22 \leq M_{R_c} \leq -18$, with a radius-dependent steepening of α for $M_{R_c} > -18$. The blue LFs contain a larger contribution from faint galaxies than the red LFs. The blue LFs have a rising faint-end component ($\alpha \sim -1.7$) for $M_{R_c} > -21$, with a weaker dependence on radius than the red LFs. The dispersion of M^* was determined to be 0.31 mag, which is comparable to the median measurement uncertainty of 0.38 mag. This suggests that the bright-end of the LF is universal in shape at the 0.3 mag level. We find that M^* is not correlated with cluster richness when using a common dynamical radius. Also, we find that M^* is weakly correlated with BM-type such that later BM-type clusters have a brighter M^*. A correlation between M^* and radius was found for the red and blue galaxies such that M^* fades towards the cluster center.

Subject headings: Galaxies: clusters: general — Galaxies: luminosity function — Galaxies: formation — Galaxies: evolution

1. INTRODUCTION

The study of the formation and evolution of galaxies is a fundamental avenue of research in the process of understanding astrophysical and cosmological issues. How galaxies form and evolve can be studied using a variety of techniques, one of those being the galaxy luminosity function (LF). The galaxy LF, assuming that galaxy mass-to-light ratios are nearly constant for similar types of galaxies, can potentially provide a direct link to the initial mass function and hence the distribution of density perturbations that are thought to give rise to galaxies (Press & Schecter 1974). Since most galaxies are not isolated entities, evolutionary processes, in addition to those expected for an aging stellar population, can occur as galaxies interact with their environment.

The galaxy LF — the number of galaxies per unit volume in the luminosity interval L to $L+dL$ — can be used as a diagnostic tool to search for changes in the galaxy population. In particular, the LF for cluster galaxies can help ascertain the influence of the cluster environment on the galaxy population. For example, a change in the shape of the LF with respect to cluster-centric radius provides important insight into the dynamical processes at work in the cluster environment.

A central theme in the early studies of the galaxy cluster LF has been to determine whether the LF is universal in shape (e.g., Hubble 1936; Abell 1962; Oemler 1974).

While introducing the modern form of the LF, the so-called "Schechter Function", Schechter (1976) suggested that the cluster LF is universal in shape, and can be characterized with a turnover of $M_B^* = -20.6 + 5\log h_{50}$ and a faint-end slope of $\alpha = -1.25$. Further support for a universal LF has been provided by several studies such as Lugger (1986), Colless (1989), Gaidos (1997), Yagi et al. (2002), and De Propris et al. (2003). In contrast, several studies have shown that the shape of the cluster LF is not universal (e.g., Godwin & Peach 1977; Dressler 1978; López-Cruz et al. 1997; Piranomonte et al. 2001; Hansen et al. 2005; Popesso et al. 2006). One expects that the LF depends on cluster-centric radius since the mixture of galaxy morphological types should vary with radius, as implied by the morphology–density relation (Dressler 1980). Since different morphological types are characterized by different LFs (Binggeli et al. 1988) the cluster LF (integrated over all galaxy types) should not be universal. Indeed, some studies have provided evidence that the cluster LF does vary with cluster-centric radius (e.g., Beijersbergen et al. 2002a; Goto et al. 2005; Hansen et al. 2005; Popesso et al. 2006).

The main goal of this paper is to investigate the change in the cluster R_c-band LF as a function of cluster-centric radius. To avoid the inherent bias that has plagued numerous studies, the cluster LF will be compared based on scaling relative to the dynamical radius, r_{200}. The use of a dynamical radius for comparing galaxy populations for a sample of clusters, provides one of the most robust, least-biased, photometric survey yet published on the LF of Abell clusters. Directly comparing LFs that sample only the cluster core region with other cluster LFs that extend to the outskirts, will suffer from radial sampling bias given that the shape of the LF has been shown to depend on cluster-centric radius (e.g., Christlein & Zabludoff 2003; Hansen et al. 2005;

[1] Department of Astronomy, University of Illinois, Urbana, IL 61801; email: wbark@astro.uiuc.edu
[2] Department of Astronomy and Astrophysics, University of Toronto, Toronto, ON, Canada, M5S 3H4; email: hyee@astro.utoronto.ca
[3] Instituto Nacional de Astrofísica, Optica y Electrónica, Tonantzintla, Pue., México; email: omarlx@inaoep.mx
[4] Visiting Astronomer, Kitt Peak National Observatory. KPNO is operated by AURA, Inc. under contract to the National Science Foundation.

Popesso et al. 2006). A direct comparison of the galaxy population with respect to cluster-centric radius based on r_{200}, will help to accurately measure the change in the properties of cluster galaxies as a function of global environment. These data will also provide information to help settle the long-standing debate regarding the universality of the cluster galaxy LF and the properties of the faint dwarf galaxy component.

This paper is the third in a series resulting from a multi-color imaging survey of low-redshift ($0.02 \leq z \leq 0.2$) Abell clusters. The paper is organized as follows. In §2 we present a brief overview of the sample selection and data reduction procedure. In §3 we describe the methodology for generating the galaxy cluster LF. In §4 we examine the LF for different color-selected galaxy populations of our cluster sample. Discussion and conclusions are presented in §5. Finally, various selection effects and biases are explored in the Appendix. Further details regarding sample selection, observations, image pre-processing, catalogs, and finding charts can be found in López-Cruz (1997), Barkhouse (2003), and Barkhouse et al. (2007a; in preparation, Paper I of this series). A detailed discussion of the color-magnitude relation (CMR) of early-type galaxies using this survey can be found in Paper II (López-Cruz et al. 2004). Paper IV characteristics the cluster galaxy luminosity and color distribution by examining the dwarf-to-giant ratio and the galaxy red-to-blue count ratio (Barkhouse et al. 2007b, in preparation). Recent observations suggest that the best cosmological model is characterized by $\Omega_M \simeq 0.3$, $\Omega_\lambda \simeq 0.7$, and $H_0 \simeq 70$ km s^{-1} Mpc^{-1} (e.g., Spergel et al. 2003). Since the effects of curvature and dark energy are negligible at low-redshifts ($z < 0.2$) and to allow direct comparisons with previous studies, we have set for convenience, unless otherwise indicated, $H_0 = 50$ km s^{-1} Mpc^{-1} and $q_0 = 0$ throughout this paper.

2. OBSERVATIONS AND DATA REDUCTIONS

The galaxy cluster sample utilized for this paper is identical to that described in Paper II of this series (López-Cruz et al. 2004). We summarize the observations and data reductions below.

The galaxy cluster sample is composed of Abell clusters selected mainly from the X-ray compilation of Jones & Forman (1999). The primary cluster sample was selected based on the following criteria; (1) clusters should be at high galactic latitude, $|b| \geq 30°$; (2) their redshifts should lie within the range $0.04 \leq z \leq 0.20$; (3) the Abell richness class (ARC) should, preferably, be > 0; and (4) the declination $\delta \geq -20°$. Some ARC = 0 clusters were included in the final sample due to the lack of suitable clusters at certain right ascensions during the observations. This sample includes 47 clusters of galaxies observed in B, and Kron-Cousins R_c and I at KPNO with the 0.9 m telescope using the 2048×2048 pixel T2KA CCD ($0.68''$ pixel^{-1}) (López-Cruz 1997; Yee & López-Cruz 1999; López-Cruz 2001, hereafter the LOCOS sample; López-Cruz et al. 2007, in preparation).

A sub-sample of eight clusters from Barkhouse (2003) is included to complement our 47-cluster sample by covering the low-redshift interval from $0.02 \leq z \leq 0.04$. These data were obtained at KPNO with the 0.9 m telescope using the 8K MOSAIC camera (8192×8192 pix-

els; $0.423''$ pixel^{-1}). The clusters for this sample were selected using the previous criteria except that ARC = 0 clusters were not preferentially excluded. In addition, two clusters imaged in B and R_c are included from Brown (1997) using the same instrumental setup as the LOCOS sample and selection criteria as the MOSAIC data. All clusters in the sample are detected in X-rays and are found to have a prominent CMR (López-Cruz et al. 2004).

The integration times for our 57-cluster sample varies from 250 to 9900 s, depending on the filter and the redshift of the cluster (only the B- and R_c-band data are considered here). Control fields are also an integral part of this survey. For this study we use a total of six control fields in both the B and R_c filters. The control fields were chosen at random positions on the sky at least 5° away from the clusters in our sample. These control fields were observed using the MOSAIC camera to a comparable depth and reduced in the same manner as the cluster data. All observations included in this study were carried out during 1992-1993 and 1996-1998.

Processing of the 8k mosaic images were done using the `mscred` package within the IRAF environment. The photometric reduction was carried out using the program PPP (Picture Processing Package; Yee 1991), which includes algorithms for performing automatic object finding, star/galaxy classification, and total magnitude determination. A series of improvements to PPP described in Yee et al. (1996) that decreases the detection of false objects and allows star/galaxy classification in images with a variable point-spread-function (PSF) was utilized.

The object list for each cluster is compiled from the R_c frames. The R_c frames are chosen because they are deeper than the images from the other filters. Galaxy *total magnitudes* are measured with PPP using a curve-of-growth analysis. The maximum aperture size ranged from $20''$ for faint galaxies ($R_c > 18.5$) to as large as $120''$ for cD galaxies in $z \sim 0.02$ clusters. An optimal aperture size for each object is determined based on the shape of the curve-of-growth using criteria described in Yee (1991). The photometry of galaxies near the cluster core was carried out after the cD and bright early-type galaxies had been removed using profile-modeling techniques developed by Brown (1997).

Galaxy colors were determined using fixed apertures of $11.0\,h_{50}^{-1}$ kpc on the images of each filter at the redshift of the cluster, sampling identical regions of galaxies in different filters, while imposing a minimum color aperture of ~ 3 times the full-width-half-maximum (FWHM) in order to avoid seeing effects (average seeing $\sim 1.5''$). The overall internal accuracy in the color determinations is ~ 0.005 mag in $B - R_c$ for bright objects. The errors for faint objects can be as large as 0.5 mag in $B-R_c$. We note that the total magnitude of a galaxy is determined using the growth curve from the R_c image, while the total magnitude in the B image is determined using the color difference with respect to the R_c image (for more details, see Yee 1991).

Star/galaxy classification was performed within PPP using a classifier that is based on the comparison of the growth curve of a given object to that of a reference PSF. The reference PSF is generated as the average of the growth curves of high signal-to-noise ratio (S/N), non-saturated stars within the frame. The classifier measures

the "compactness" of an object by effectively comparing the ratio of the fluxes of inner and outer parts of an object with respect to the reference PSF.

Instrumental magnitudes are calibrated to the Kron-Cousins system by observing standard stars from Landolt (1992). Due to the large field, up to 45 standard stars can be accommodated in a single frame. The color properties of the standard stars cover a large color range that encompasses those of elliptical and spiral galaxies. The standard stars are measured using a fixed aperture of 30 pixels for the LOCOS frames and 32 pixels for the MO-SAIC data. These aperture sizes are selected as being the most stable after measuring the magnitudes using a series of diameters. We adopt the average extinction coefficients for KPNO and fit for the zero points and color terms. The rms in the residuals of individual fittings is in the range $0.020 - 0.040$ mag, which is comparable to the night-to-night scatter in the zero points. This can be considered as the systematic calibration uncertainty of the data.

The final galaxy catalogs were generated using the information and corrections derived previously. For data obtained under non-photometric conditions, single cluster images were obtained during photometric nights in order to calibrate the photometry (three clusters in total). The completeness limit for each field is based on a fiducial 5σ limit determined by calculating the magnitude of a stellar object with a brightness equivalent to having a $S/N = 5$ in an aperture of $2''$. This is done by scaling a bright unsaturated star in the field to the 5σ level. Since the 5σ limit is fainter than the peak of the galaxy count curve, and hence below the 100% completeness limit for galaxies, a conservative 100% completeness limit is in general reached at $0.6 - 1.0$ mag brighter than the 5σ detection. See Yee (1991) for a detailed discussion of the completeness limit relative to the 5σ detection limit.

Galaxy colors and magnitudes were corrected for the extinction produced by our Galaxy. The values of the Galactic extinction coefficients were calculated from the Burstein & Heiles (1982) maps using the reported $E(B - V)$ values, or directly from the A_B tabulations for bright galaxies (Burstein & Heiles 1984) with coordinates in the vicinity of our pointed observations using NED. Extinction values used for each cluster are provided in Paper I.

3. THE LUMINOSITY FUNCTION

3.1. Fitting the Schechter Function

The galaxy cluster LF in modern times has mainly been parameterized using the Schechter function (Schechter 1976). This function has the form

$$\phi(L)\,dL = \phi^*(L/L^*)^\alpha \exp(-L/L^*)\,d(L/L^*), \qquad (1)$$

where $\phi(L)\,dL$ is the number of galaxies per unit volume in the luminosity interval L to $L + dL$, ϕ^* is the number per unit volume, and L^* is the "characteristic" luminosity. This function is characterized by having an exponential shape at the bright-end and a power-law like feature, whose slope is measured by α, at the faint-end (for example, see Figure 1). By introducing the change of variables $M - M^* = -2.5\log(L/L^*)$, equation 1 can

be written in terms of absolute magnitude as

$$n(M)\,dM = kN^* e^{[k(\alpha+1)(M^*-M)-\exp\{k(M^*-M)\}]}dM, \tag{2}$$

where $k = 0.4\ln 10$ (cf., Colless 1989).

The Schechter function is fit to the cluster galaxy counts following the procedure in López-Cruz (1997). In summary, the function parameters M^*, N^*, and α are estimated by performing a χ^2 minimization of the form

$$\chi^2 = \sum_i \frac{(N_i - N_i^e)^2}{\sigma_i^2}, \tag{3}$$

where N_i is the net galaxy counts in the ith bin of the observed LF, N_i^e is the expected number of counts in the ith bin of width ΔM, and σ_i is the uncertainty of the counts in the ith data bin. The expected number of counts in the ith bin, corrected for the loss of information due to the finite bin size, is given by (Schechter 1976)

$$N_i^e = n(M_i)\,\Delta M + n_i''(M_i)\,\Delta M^3/24, \tag{4}$$

where the derivative is with respect to absolute magnitude, and ΔM is the bin width. This correction is derived by Taylor-expanding $n(M)$ to a third order about the bin's center and integrating $N_i^e = \int_{M-\frac{1}{2}\Delta M}^{M+\frac{1}{2}\Delta M} n(M)dM$. The uncertainty, σ_i, is taken to be (cf., Lugger 1986)

$$\sigma_i = [(N_i^e + N_{bi}) + 1.69\,N_{bi}^2]^{1/2}, \tag{5}$$

where N_{bi} is the background counts in the ith bin, $(N_i^e + N_{bi})^{1/2}$ is the Poisson uncertainty in the uncorrected LF counts, and the second term in the square root expression is the measured field-to-field variation per bin in the background field counts (see §3.2). The uncertainty of the observed net galaxy counts due to cosmic variance is thus taken into account when fitting the Schechter function. For a single Schechter function fit, N^* is fixed so that the total number of observed galaxies in the data set is equal to the number predicted by the Schechter function. The parameters M^* and α are obtained by minimizing equation 3 using the Levenberg-Marquardt method (Press et al. 1992).

3.2. Background Galaxy Correction

The R_c-band LF is constructed statistically by subtracting a background galaxy population from the cluster galaxy counts. This method, in contrast to measuring the redshift of individual galaxies in the cluster field, relies on an accurate determination of the background field population. This statistical approach has been used in numerous studies to date (e.g., Oemler 1974; Schechter 1976; Colless 1989; Driver et al. 1998; Yagi et al. 2002; Andreon et al. 2004). The modal field-to-field variation per magnitude bin has been measured to be $\sim 30\%$ above Poisson statistics among the six background fields. We use this value to approximately account for the additional uncertainty in the background counts due to field-to-field variations in equation 5. Although the use of galaxy redshifts would provide a more robust determination of the cluster LF, the relatively modest variation of the background counts, with respect to the cluster counts, makes the statistically derived cluster LF valid. A similar conclusion has also been reached by a number of independent studies (e.g., Driver et al. 1998).

Several studies have examined the effect on the derived cluster LF using a global background galaxy field correction versus one measured locally for each cluster (e.g., Goto et al. 2002; Hansen et al. 2005; Popesso et al. 2005; González et al. 2006). For example, Popesso et al. (2005) has shown for a study of 69 clusters based on SDSS DR2 data, that there is no significant difference in the measured cluster LF using either a global or local background subtraction technique.

Contamination from the 2-d projection on the sky of a distant cluster in the field-of-view of the target cluster can prove to be problematic by skewing the LF, especially at the faint-end where galaxies from the background cluster directly add to the desired LF. Fortunately, the CMR can help minimize this contamination by identifying the early-type red sequence of the target cluster (López-Cruz et al. 2004). The effect of background clusters on the desired LF can thus be reduced by selecting an appropriate color cut, thus eliminating objects redder than the cluster red sequence. This method can also help to locate foreground clusters which, given the low redshift of our cluster sample, are not a significant concern for this study.

To minimize contamination from background galaxies, we cull galaxies that are 0.22 mag redward of the CMR (i.e., ≥ 3.0 times the average $B - R_c$ dispersion of the cluster red sequence). The dispersion of the cluster red sequences are tabulated in Table 1 of López-Cruz et al. (2004) and histogram representations of the rectified $B - R_c$ color distributions are presented in Paper I (see also Figure 1 from López-Cruz et al. 2004). In several cases (e.g., A2152), a color cut $< 3\sigma$ is used if a second red sequence from a more distant cluster (and hence at a redder $B - R_c$) is apparent in the color-magnitude diagram (CMD) of the target cluster. For faint magnitudes, we cull galaxies redder than $2.5\sigma_{B-R_c}$ if 2.5 times the average uncertainty in the galaxy $B - R_c$ is redder than 3.0 times the dispersion of the cluster red sequence.

3.3. K-Correction

K-corrections are applied using a single parametrization based on early-type galaxies, which dominant the cluster galaxy population Dressler (1980). At the low redshift of our sample, the difference between early- and late-type galaxies is minimal for the R_c-band. In general, the maximum K-correction applied was ~ 0.2 mag. The K-correction adopted for each cluster is tabulated in Paper I. All LFs presented in this paper have been extinction- and K-corrected, and no attempt has been made to correct for individual internal galaxy absorption.

3.4. Cluster Dynamical Radius

Studies of the properties of galaxy clusters, such as the CMR and LF, have been routinely compared on a cluster-by-cluster basis. Nearly all of these studies define a "cluster" based on the total area covered by the telescope detector (e.g., Dressler 1978; López-Cruz 1997) or by using a specific physical length (e.g., $1\,h_{100}^{-1}$ Mpc; Yagi et al. 2002). The large variation in cluster richness (Yee & López-Cruz 1999) inhibits the usefulness of the above techniques for robustly comparing cluster properties. Some authors have attempted to "normalize"

clusters by directly comparing only clusters of comparable class (e.g., Bautz-Morgan type) or by weighting each cluster according to richness (Garilli et al. 1999; Piranomonte et al. 2001; De Propris et al. 2003). The use of a variety of different methods have certainly contributed to conflicting results that have emerged from past investigations regarding measurements such as the universality of the LF (Lugger 1986; Driver et al. 1998; Popesso et al. 2006).

As a means of computing a "dynamical" radius within which cluster characteristics can be robustly compared, the r_{200} radius was calculated for each cluster. The r_{200} radius marks the size of a cluster within which the average density is 200 times the critical density, and follows from the definition used in Carlberg et al. (1997) and Yee & Ellingson (2003). The r_{200} radius is expected to contain the bulk of the virialized mass of a cluster (e.g., Cole & Lacey 1996) and is used in this study as a scaling factor to compare cluster features. The use of this type of "normalization" allows us to compare galaxy cluster populations in a less biased fashion, especially those properties which are a function of cluster richness and cluster-centric radius. This approach has recently been implemented by Hansen et al. (2005) and Popesso et al. (2006) to study the properties of a sample of clusters/groups from the SDSS.

The procedure for determining r_{200} involves the calculation of the velocity dispersion, which requires redshift measurements for a number of cluster galaxies. The data available for this study do not include redshift information for cluster members, thus an alternative method was employed to estimate r_{200} for each cluster.[5] This method relies on the correlation between B_{gc} and r_{200} as measured for the CNOC1 sample (Yee & Ellingson 2003). The B_{gc} parameter is a measure of the cluster-center galaxy correlation amplitude, and has been shown to be a robust estimator of cluster richness (Yee & López-Cruz 1999; Yee & Ellingson 2003). The measured values of B_{gc} for our cluster sample are calculated using the method outlined in Yee & López-Cruz (1999). Figure 2 depicts the relationship between r_{200} and B_{gc} for 15 clusters from the CNOC1 survey (Yee et al. 1996), adopted from Yee & Ellingson (2003). We note that the r_{200} vs. B_{gc} figure in Yee & Ellingson (see their Figure 5) used the less well-determined r'_{200} from Carlberg et al. (1997, see their Table 1). This explains the decrease in the scatter of r_{200} vs. B_{gc} for our Figure 2 compared to the corresponding figure in Yee & Ellingson. A fit to these data yields

$$\log r_{200} = (0.48 \pm 0.10) \log B_{gc} - (1.10 \pm 0.31), \quad (6)$$

where r_{200} has units of Mpc, and B_{gc} units of Mpc$^{1.8}$. The rms scatter in the derived values of r_{200} is on the order of 15%. The fit was performed using the bisector bivariate correlated errors and intrinsic scatter (BCES) estimator (Akritas & Bershady 1996) since this algorithm accounts for uncertainties in both variables. The cluster MS 1455+22 (open circle in Figure 2) was excluded from the fit since it is $\sim 3\sigma$ from the expected relation (see Yee & Ellingson 2003 for a detailed discussion of MS 1455+22).

---

[5] Only approximately 30% of the 57 clusters have published robust velocity dispersions.

The estimation of r_{200} for each cluster is accomplished by calculating the value of B_{gc} directly from the galaxy cluster photometric catalog and then applying equation 6 to determine r_{200}. Table 1 lists the values of B_{gc} and r_{200} for each cluster used in this study. The tabulated uncertainty in the value of r_{200} is calculated directly from the 15% rms scatter.

Yee & López-Cruz (1999) showed that a subset of our Abell cluster sample has a similar relationship between cluster velocity dispersion (σ_v) and B_{gc} as the CNOC1 sample, and since r_{200} is estimated from σ_v, the r_{200}–B_{gc} relation for the Abell clusters should be similar to that of the CNOC1 sample.

To test the validity of our results, we compare the values of r_{200} from Table 1 for those clusters in common with Rines et al. (2003), Miller et al. (2005), Popesso et al. (2007), and Aguerri et al. (2007). For the 3 clusters in common with Rines et al., we find a mean difference in r_{200} of -0.17 ± 0.17 Mpc (all physical length scales have been converted to our distance scale), where our values are greater on average (the rms is given as the uncertainty). For the 10 clusters in common with Miller et al., we find a mean difference of 0.73 ± 0.73 Mpc. The mean difference for the 9 clusters in common with Popesso et al. is 0.25 ± 0.32 Mpc, while the average difference for the 12 clusters in common with Aguerri et al. is -0.26 ± 0.62 Mpc. The larger discrepancy with the Miller et al. sample is due to the uncommonly large r_{200} values ($r_{200} > 4$ Mpc) for the three richest clusters. In fact, Miller et al. cautions that the radius within which the density measurements have been made to determine r_{200} may be inaccurate. We believe that the Miller et al. r_{200} values are biased-high for the more massive clusters in our comparison sample. If we restrict our analysis to the combined Rines et al., Popesso et al. and Aguerri et al. samples, we find a mean r_{200} difference of -0.07 ± 0.53 Mpc. Thus, the values of r_{200} derived via equation 7 are reasonable. (See the discussion in §A.5 regarding the effect on the derived LF for a 15% scatter in r_{200}.)

4. RESULTS

4.1. Individual Cluster Luminosity Functions

The R_c-band LFs for the 57 clusters presented in this paper are depicted in Figure 1 for galaxies brighter than the 100% completeness limit. To help facilitate the comparison between clusters, the LFs are generated using galaxy counts within a radius of $(r/r_{200}) \leq 0.4$ from each cluster center. The cluster center is normally selected using the brightest cluster galaxy (BCG) or, when some doubt exists, the brightest early-type galaxy that is closest to the X-ray centroid as given, for example, by Jones & Forman (1999). Figure 1 includes the R_c-band LF for A496 and A1142 from data obtained by Brown (1997). The small size of the detector (2k×2k) and the low redshift, limits the LF coverage to within a cluster-centric radius of $(r/r_{200}) \leq 0.2$ for Abell 496 and $(r/r_{200}) \leq 0.3$ for Abell 1142.

The cluster LFs presented in Figure 1 have each been fit with a Schechter function in the range $-24 \leq M_{R_c} \leq -20$, with the faint-end slope fixed at $\alpha = -1$. This has been done to help serve as a reference point for comparing individual clusters. The fitted value of M^* for each cluster is tabulated in Table 1 and the best-fit Schechter function is represented by the solid line in

Figure 1. The fitting of the LFs does not include the BCG. The presence of these galaxies is easily noticed by their affect on the brightest magnitude bin, whose value is usually offset from the best-fit Schechter function. Schechter (1976) remarked that BCGs do not seem to be a natural extension of the cluster LF (see also, Sandage 1976; Dressler 1978; Loh & Strauss 2006). A fit to his composite LF for a sample of 13 clusters was more robust when the BCG was excluded from each cluster. This has led to numerous debates on the formation mechanism of BCGs (e.g., Geller & Peebles 1976; Bhavsar 1989; Bernstein & Bhavsar 2001). Since most studies of cluster LFs exclude the BCG from the LF fit, BCGs will not be included in subsequent LF analysis unless otherwise noted (see additional discussion in §A.6).

Visual inspection of the individual cluster LFs in Figure 1 indicates that, in general, the bright-end appears to be well-fit by a Schechter function, with a rising faint-end ($M_{R_c} \gtrsim -19$) of various strength. The presence of a "flat" LF ($\alpha = -1.0$) at the faint-end usually occurs for clusters in which the uncertainty in the net galaxy counts at the faint-end is large, or the LF has not been sampled to a sufficient depth to reveal a rising faint-end component, although we can not rule out intrinsically flat LF clusters.

An additional feature, visible for several cluster LFs, is a "dip" in the galaxy counts at $-20 \lesssim M_{R_c} \lesssim -19$. This characteristic is most-prominent for A84, A154, A634, A690, A1291, A1569, A1656, A1795, A2384, and A2556. A possible cause of this feature is the variation in the ratio of galaxy types that comprise the individual cluster galaxy population. This may result from the fact that the elliptical and spiral galaxy LF is better described using a Gaussian function, while the dwarf galaxy LF is "Schechter-like" in shape (Binggeli et al. 1988).

4.2. Composite Luminosity Function
4.2.1. Total Luminosity Function

The statistical subtraction of a background galaxy population can drastically affect the accuracy of determining the shape of the cluster LF when the net number of cluster galaxies is small. Generally, this will be an important factor for galaxies located in the outskirts of clusters. To reduce the uncertainty in the shape of the LF at large cluster-centric radii, cluster galaxy counts have been combined to form a composite LF. This also averages out any apparent variations in the shape of the individual LFs due to cosmic variance in the background counts. To provide an adequate coverage of the faint-end of the LF, we have selected a sub-sample of 29 clusters for the composite LF that are 100% complete to $M_{R_c} = -16.5$ (absolute R_c-band completeness limits, $M_{R_c}^{Com}$, are tabulated in Table 1). Following the procedure for combining cluster counts in adjacent magnitude bins (Schechter 1976), clusters complete to $M_{R_c} = -17.0$ (13 additional ones) are also included in our composite LF. This has been accomplished by scaling the number of net galaxy counts in the faintest magnitude bin ($-17.0 \leq M_{R_c} \leq -16.5$) by the ratio ($N_2/N_1$); where N_1 is the total net galaxy count to $M_{R_c} = -17.0$ for the 29 clusters complete to at least $M_{R_c} = -16.5$, and N_2 is the total net galaxy count to $M_{R_c} = -17.0$ for the 42 clusters complete to at least $M_{R_c} = -17.0$. By following

this method, we are able to construct a composite LF which is complete to $M_{R_c} = -16.5$ and contains galaxy counts from 42 individual clusters.

To search for differences in the LF which may correlate with cluster properties, we present the composite R_c-band LF in Figure 3 for four different radial bins, centered on the BCG, extending out to $(r/r_{200}) = 1$. Examination of Figure 3 clearly shows that a single Schechter function is inadequate to fully describe the shape of the composite LF at any radius. The sum of two Schechter functions has therefore been used to model the shape of the LF, with the resultant fit given by the solid line in Figure 3.

Several recent studies have determined that the sum of two Schechter functions provides a more adequate fit to the cluster LF than a single Schechter function (e.g., Driver et al. 1994; Hilker et al. 2003; González et al. 2006; Popesso et al. 2006). Alternative LF fitting functions include a Gaussian for the bright-end and a single Schechter function for the faint-end (e.g., Thompson & Gregory 1993; Biviano et al. 1995; Parolin et al. 2003), a single power-law fit to the faint-end (e.g., Trentham et al. 2001), and an Erlang plus a Schechter function (Biviano et al. 1995).

For Figure 3, a single Schechter function was first fit to the bright-end from $-24 \le M_{R_c} \le -20$, and a second Schechter function from $-24 \le M_{R_c} \le -16.5$. Due to the degeneracy involved in fitting two Schechter functions, the faint-end slope of the first Schechter function (for the bright-end) was fixed at $\alpha_1 = -1.0$. This procedure is justified since a fit to all 57 clusters for $-24 \le M_{R_c} \le -20$ yields $\alpha = -0.96 \pm 0.04$. Limiting the analysis to the 42 clusters used to form the composite LF gives $\alpha = -0.95 \pm 0.05$. In addition, we imposed a second constraint that $N_2^* = 2N_1^*$, where N_1^* and N_2^* are the scale factors of the Schechter function fit to the bright- and faint-end of the LFs, respectively. When N_1^* and N_2^* are free to vary, we find that the geometric mean of the ratio $(N_2^*/N_1^*) = 2.12$ when measured over the four radial bins from $(r/r_{200}) = 0.0$ to 1.0. Due to the relatively bright absolute magnitude limits (-16.5) and the strong coupling of the Schechter function parameters, we have chosen to derive the faint-end slope α as the primary parameter of interest and thus set $(N_2^*/N_1^*) = 2$.

The resultant Schechter function fit parameters for the composite LFs are tabulated in Table 2, along with the 1σ uncertainties, where M_1^* and M_2^* are the turnover in the bright and faint Schechter functions, respectively. Since the faint-end slope of the first function has been fixed at $\alpha_1 = -1.0$, only α_2 is presented. The individual clusters that comprise the sample of 42 clusters used to construct the composite LF cover various fractions of (r/r_{200}). This results in a different number of clusters contributing to the LF counts in each of the four separate radial bins (see column 7 from Table 2).

Examination of Figure 3 and Table 2 clearly indicates that the faint-end slope tends to become steeper as cluster-centric distance increases. The faint-end slope is significantly steeper, as measured out to $(r/r_{200}) = 1$, than the traditional value of $\alpha = -1.25$ (Schechter 1976). To facilitate the comparison between the different LFs, the LF for each of the four radial bins has been plotted together in Figure 4. The outer three LFs, $0.2 \le (r/r_{200}) \le 1.0$, have been scaled to match the

counts of the inner-most LF in the $-22 \le M_{R_c} \le -21$ magnitude range. This figure clearly demonstrates the trend of a steepening of the faint-end slope with increasing cluster-centric radius.

To determine what effect imposing the constraint $(N_2^*/N_1^*) = 2$ has on the robustness of the measured radial-dependent change in the faint-end slope, we refit our LFs by allowing N_1^* and N_2^* to vary. Due to the degenerate nature of fitting for N^*, M^* and α simultaneously, we measure the ratio (N_2^*/N_1^*) for the total cluster sample from four annuli by; i) fixing $\alpha_2 = -2.01$, $M_1^* = -22.31$ (mean values averaged over radial bins) and $\alpha_1 = -1.0$, and then solving for N_1^*, N_2^* and M_2^*, and ii) fixing $M_2^* = -18.04$, $M_1^* = -22.31$ (mean values averaged over radial bins) and $\alpha_1 = -1.0$, and then solving for N_1^*, N_2^* and α_2. The increase in the steepness of the faint-end slope with increasing cluster-centric radius will be manifest by an increase in the (N_2^*/N_1^*) ratio with increasing radius.

For case (i) we find that the ratio $(N_2^*/N_1^*) = (0.49, 0.50, 5.10, 13.00)$ for $(r/r_{200}) = (0.0 - 0.2, 0.2 - 0.4, 0.4 - 0.6, 0.6 - 1.0)$. For case (ii) we measure $(N_2^*/N_1^*) = (0.85, 2.76, 2.60, 4.19)$ for $(r/r_{200}) = (0.0 - 0.2, 0.2 - 0.4, 0.4 - 0.6, 0.6 - 1.0)$. These results are consistent with the increase in the steepness of the faint-end slope with increasing radius. Due to the degeneracy in fitting the LF, the relative fraction of bright and faint cluster galaxies can be best studied by integrating over the respective LFs. This will be discussed in detail in the context of the dwarf-to-giant ratio of red- and blue-selected galaxies in Paper IV of this series.

We compare our composite LF with two recent studies by converting to R_c using Fukugita et al. (1995) and adopting our distance scale. González et al. (2006) used a double Schechter function to characterize the composite LF of 728 groups/clusters selected from SDSS DR3. They find $M^* = -23.12 \pm 0.12$ with $\alpha = -1.89 \pm 0.04$ for galaxies selected within 1.0 Mpc of the group center. Dividing their sample into two radial bins (0.0–0.6 and 0.6–1.2 Mpc), González et al. determined that M^* gets brighter with increasing radius (-22.9 ± 0.2 to -23.5 ± 0.2), while the faint-end slope becomes steeper ($\alpha = -1.80 \pm 0.03$ to $\alpha = -1.99 \pm 0.03$). The measured range in M^* for this study is significantly brighter ($\sim 0.6 - 1.1$ mag) than our results tabulated in Table 2. This may be related to the fact that the González et al. sample consists predominately of group systems. For the faint-end, the measured slope values are consistent with our results, including the trend for a steepening of α with increasing radius.

Popesso et al. (2006) studied the composite LF of 69 clusters from the *ROSAT* All Sky Survey/SDSS galaxy cluster catalog (RASS-SDSS) using the sum of two Schechter functions. The faint-end slope was found to increase from $\alpha = -2.02 \pm 0.06$ to -2.19 ± 0.09 when the sampling radius increased from r_{500} to r_{200}. This compares well with our measured range in α even though we use annuli to determine α rather than a circular region with a changing radius. For the bright-end LF, Popesso et al. finds α varies from -1.05 ± 0.07 for r_{500} to -1.09 ± 0.09 for r_{200}. This result is consistent with our use of a fixed $\alpha_1 = -1.0$. Also, M^* of the bright-end was found to brighten slightly from $M_{R_c} = -22.54 \pm 0.13$ at r_{500} to $M_{R_c} = -22.64 \pm 0.16$ for r_{200}. These re-

sults are consistent within 1σ of our measured values of -22.26 ± 0.06 and -22.38 ± 0.15 for the inner- and outer-most radial bin, respectively. In addition, we also detect a slight brightening of M^* with increasing cluster-centric radius as reported by Popesso et al. for their sample.

4.2.2. *Red Sequence Luminosity Function*

To explore the dependency of the composite LF on the physical properties of cluster galaxies such as color, the cluster galaxy catalogs have been divided into various sub-samples that populate different regions of the CMD.

The composite LF of galaxies located on the red sequence of the CMR was constructed by selecting galaxies using the following criteria: 1) galaxies are selected if they are within ±3.0 times the average dispersion of the Gaussian fit to the CMR (i.e., ±0.22 mag; López-Cruz et al. 2004) or, depending on which is greater, 2) within 2.5 times the average uncertainty in the galaxy $B - R_c$ color redward of the red sequence fit (see Figure 5). In practice, galaxies at the bright-end of the red sequence will be selected according to the first criterion; as fainter galaxies are chosen, the uncertainty in the $B - R_c$ color will increase to a value where galaxies will be selected via criterion 2.

The first criterion defines the loci of the red sequence in the CMD. The second criterion helps insure that faint red sequence galaxies near the completeness limit are selected, even though they will be scattered further from the CMR than the limit imposed by criterion 1 due to the increased uncertainty in the measured color. As stated in the second criterion, only galaxies redward of the CMR were chosen. This was implemented to minimize the inclusion of galaxies blueward of the red sequence (what we refer to as the "blue" galaxy population), which are scattered into the red sequence region due to the color uncertainty at faint magnitudes. To compensate for the "missing" members of the red galaxy population that are located blueward of the red sequence, the net galaxy counts for those galaxies fainter than the magnitude at which objects are culled based on criterion 2, have been increased by a factor of two, since in the absence of a blue galaxy population one might expect the red sequence members to be symmetrically distributed on either side of the CMR.

Figure 5 illustrates the region of the CMD where red sequence galaxies have been selected for Abell 260. For galaxies brighter than $R_c = 18.8$ (indicated by the vertical dashed line), the $2.5\sigma_{B-R_c}$ is less than 3.0 times the average dispersion of the red sequence (0.22 mag), thus galaxies are chosen according to criterion 1. For galaxies fainter than $R_c = 18.8$, the uncertainty in the color measurement invokes selection by criterion 2. As depicted in Figure 5, only galaxies redder than the red sequence are selected for magnitudes fainter than $R_c = 18.8$ mag.

The net red sequence galaxy counts were calculated by subtracting the background field counts from the "raw" red galaxy counts. The background field galaxies were selected using identical color cuts as imposed on the red sequence galaxy sample.

The composite red sequence galaxy LF for four different radial bins (same annuli as that used for the total composite LF) is depicted in Figure 6. The LFs have been constructed by scaling and combining clusters, complete to $M_{R_c} = -16.5$, using the same method as that described for the total composite LF (§4.2.1). Visual inspection of the red sequence LFs shows that a single Schechter function, in general, would provide a reasonable fit to the overall shape of the LF except for the faintest magnitude bins. To compare the red sequence LF to the total LF, we fit the sum of two Schechter functions to the red sequence LFs. By allowing N_1^* and N_2^* to vary, we find that the geometric mean of the ratio (N_2^*/N_1^*)=0.4, averaged over the four radial bins. We thus impose that (N_2^*/N_1^*)=0.4 and fit for M_1^*, M_2^*, and α_2. These fits are depicted in Figure 6 and the best-fit parameters tabulated in Table 3. We note that the LF fit to the faint component for the inner-most region is poorly constrained due to the lack of data points from the rising faint-end slope. We also find that when holding M_2^* fixed and allowing (N_2^*/N_1^*) and α_2 to vary, (N_2^*/N_1^*) increases with increasing cluster-centric radius.

In Figure 7 the four red sequence LFs have been superimposed by scaling the outer three LFs to match the inner-most LF in the magnitude range $-22 \leq M_{R_c} \leq -21$. All four LFs appear to be equivalent to each other for magnitudes brighter than $M_{R_c} \simeq -18$. For magnitudes fainter than $M_{R_c} \simeq -18$, the inner-most LF appears to contain the smallest contribution from the faint galaxy component. In addition, a dip in the LF at $M_{R_c} \sim -18$ is apparent for all four radial bins (see also Figure 6).

The red sequence LFs depicted in Figure 7 are remarkably similar in shape to the composite LF for galaxies selected as having an $r^{1/4}$-like surface brightness profile given in Yagi et al. (2002) (see their Figure 7). This is not unexpected since the red sequence is dominated by early-type galaxies whose surface brightness distribution can be approximated by an $r^{1/4}$-like profile. The Yagi et al. composite LF is sampled to $M_{R_c} \sim -16.5$, for our adopted cosmology, and thus compares directly with the red sequence LFs presented in this paper. An upturn in the red sequence LF at the faint-end is present in our sample (see Figure 6 and 7) and in the composite $r^{1/4}$ LF from Yagi et al. This upturn may be the result of scattering from the blue galaxy population; however, if this is the case, the scattered galaxies must also contaminate the sample of $r^{1/4}$-like surface brightness profiles measured by Yagi et al., which seems unlikely.

In addition to Yagi et al. (2002), we also compare our red sequence LFs with the 2dF Galaxy Redshift Survey cluster sample from De Propris et al. (2003). This study presents composite LFs for a sample of 60 clusters based on the selection of galaxies relative to a classification parameter derived from the principal component analysis of spectra from Madgwick et al. (2002). LFs are constructed for early-, mid-, and late-type classes, with spectral classification based on star formation rates rather than morphological type. Assuming that the early-type spectral class is associated with red sequence cluster galaxies, we compare our results from Table 3 with De Propris et al. A single Schechter function fit to the early-type LF yields $M_{b_J}^* = -20.04\pm0.09$ and $\alpha = -1.05\pm0.04$ for $M_{b_J} < -15$. Converting to R_c and using our distance scale, we find $M_{R_c}^* = -22.92\pm0.09$ for $M_{R_c} \lesssim -18$. Since De Propris et al. samples galaxies out to 3.0 Mpc, we compare our value for M^* measured in the outer-most radial bin. From Table 3 we have $M_{R_c}^* = -22.61 \pm 0.19$,

which is within 1.5σ of the De Propris et al. result. The De Propris et al. faint-end slope, $\alpha = -1.05 \pm 0.04$, is consistent with the value of $\alpha = -1.0$ that we assume for the bright-end Schechter function given that De Propris et al. only samples to $M_{R_c} \sim -18$. Examination of our Figure 7 indicates that α becomes steeper for magnitudes fainter than -18. Thus, De Propris et al. does not probe faint enough to sample the increasing faint galaxy component.

In §4.2.1 we compared our total composite LF with Popesso et al. (2006). That study also presents the composite LF for early-type cluster galaxies based on selecting galaxies with $2.22 \leq u - r \leq 3$. Converting to R_c and our distance scale, Popesso et al. finds $M^*_{R_c} = -22.27 \pm 0.14$, with a faint-end slope of $\alpha = -2.01 \pm 0.11$ for galaxies measured within r_{200}. Our M^* values range from -22.28 ± 0.07 to -22.61 ± 0.19, thus we are in good agreement with Popesso et al. given that we measure LFs in a series of concentric annuli. The faint-end slope of Popesso et al. is flatter than our values tabulated in Table 3 ($-5.26 \leq \alpha \leq -2.83$). This discrepancy is most-likely due to the poor fit at the faint-end of our LFs as indicated by the large reduced-χ^2 values in Table 3. In fact, Popesso et al. samples $\gtrsim 1$ mag deeper than our data set, and thus is able to place a better constraint on the faint-end slope. We also note that the rise in the faint-end slope of the early-type LF from Popesso et al. occurs at approximately the same magnitude as our study ($M_{R_c} \sim -18.5$).

4.2.3. *Blue Galaxy Luminosity Function*

We construct the LF of blue cluster galaxies by selecting galaxies in the CMD blueward of the red galaxy sample. The selection of the galaxies is illustrated in Figure 8, using Abell 260 as an example. Here, galaxies brighter than $R_c = 18.8$ are designated as blue galaxies if their $B - R_c$ color is bluer than the blueward limit used to select the red sequence population. The color criterion for blue galaxies at M^* is $B - R_c = 1.4$ for Abell 260. This corresponds to an Sab-type galaxy using $B - R_c$ galaxy colors tabulated in Fukugita et al. (1995). Galaxies fainter than $R_c = 18.8$ mag are selected if they are located in the region of the CMD that is bluer than the area used to select the red sequence galaxies and brighter than the completeness magnitude. An additional correction to the galaxy counts is made by subtracting the net red sequence galaxy counts (measured from the region of the CMD fainter than $R_c = 18.8$) from the net blue cluster galaxy counts.[6] This correction is necessary to account for the red sequence galaxies that inhabit the region in the CMD that is bluer than the area used to select the red galaxy population at the faint-end.

The blue galaxy LF for four different annuli (same radial bins as that used for the total and red composite LFs) is depicted in Figure 9. The LFs have been constructed by scaling and combining clusters, complete to $M_{R_c} = -16.5$, as described previously for the total and red sequence LFs. As determined for the total and red sequence LFs, a single Schechter function is unable to

---

[6] The net blue cluster galaxy counts were calculated by subtracting background field galaxies, selected using the same color criteria as the blue cluster galaxy population, from the raw blue cluster galaxy counts.

adequately describe the shape of the blue galaxy LF. A sum of two Schechter functions (solid line in Figure 9) is fit to the blue LFs, with the best-fit Schechter parameters given in Table 4. For the LF fit procedure we set $(N^*_2/N^*_1)=3$, which is equal to the geometric mean of the ratio averaged over all four radial bins when N^*_1 and N^*_2 are allowed to vary.

In Figure 10 the blue LFs have been superimposed by scaling the outer three LFs to match the inner-most LF in the magnitude range $-22 \leq M_{R_c} \leq -21$. In general, all four LFs appear to be very similar in shape, with a slight tendency for a steeper faint-end slope at a larger cluster-centric distance. This trend can be ascertained by examining the value of α_2 measured for the four LFs (see Table 4). We note that if we fix M^*_2 and solve for (N^*_2/N^*_1) and α_2, (N^*_2/N^*_1) decreases slightly with increasing cluster-centric radius. We also note that the blue LFs are similar in shape to the composite LF composed of galaxies having an exponential-like surface brightness profile from Yagi et al. (2002) (see their Figure 9).

Analogous to the comparison of our red sequence LF with De Propris et al. (2003) and Popesso et al. (2006) in §4.2.2, we also compare our blue LF with the late-type LFs presented in these studies. Correcting for filter and cosmology difference, the single Schechter function fit to the late-type LF (Type 3+4) from De Propris et al. yields $M^*_{R_c} = -22.02 \pm 0.19$ with $\alpha = -1.30 \pm 0.10$. This value for M^* agrees well with our measured range ($-21.96 \leq M^* \leq -21.81$), while our faint-end slope is much steeper ($-1.62 \leq \alpha \leq -1.82$). As described in §4.2.2, the De Propris et al. study does not probe the faint-end of the LF to the same depth as our study ($\Delta M \sim 1.5$ mag). The fit of the faint-end slope is further complicated by the large completeness corrections required for the faintest two magnitude bins. Thus, it is not surprising that the faint-end slope of the late-type LF from De Propris et al. is flatter than our value tabulated in Table 4. The trend of a steeper α for late-type galaxies compared to early-type systems, is consistent with our results for blue versus red galaxies.

Popesso et al. (2006) presents the late-type composite LF constructed by selecting galaxies with $u - r \leq 2.22$ for a sampling radius of r_{200}. Unlike our results for the blue LF, a single Schechter function is found to be an adequate fit to the late-type LF. Converting the SDSS r-band to R_c and employing our distance scale, the late-type LF from Popesso et al. has $M^*_{R_c} = -23.41 \pm 0.52$ and $\alpha = -1.87 \pm 0.04$. The value of M^* from Popesso et al. is significantly brighter (~ 1.5 mag; 2.7σ level) than the average value measured for our blue LF. The Popesso et al. result is also ~ 1.4 mag brighter (2.5σ level) then De Propris et al. for their late-type LF, and ~ 0.8 mag brighter than the exponential composite LF from Yagi et al. (2002). We also note, based on De Propris et al., Yagi et al., and this study, that M^* is brighter for the red (early-type, $r^{1/4}$-like) LF than for the blue (late-type, exp-like) LF. This is not the case for Popesso et al., where the early-type LF has a fainter M^* (~ 1.1 mag) than the late-type LF. We do not understand this discrepancy, but speculate that it may be due to the selection of galaxy types by Popesso et al. based on $u-r$ color. The faint-end slope of the Popesso et al. late-type

LF ($\alpha = -1.87 \pm 0.04$) is consistent with the range in slope values measured for our blue LF (-1.62 ± 0.05 to -1.82 ± 0.10).

In Figure 11 the total, red sequence, and blue LFs for the four radial bins are directly compared. To aid this comparison, the red sequence and blue LFs have been matched to the total LF in each radial bin by scaling the red and blue galaxy counts such that the number of galaxies between $-24 \leq M_{R_c} \leq -16.5$ is equal to the total LF in the same magnitude range. Inspection of Figure 11 shows that the total and red sequence LFs are composed of a bright galaxy component that is much more significant than the contribution from the blue LFs. For the faint-end, the blue galaxy sample appears to contribute the greatest fraction of the faint dwarf galaxy population, with the largest difference apparent for the inner-most radial bin where $(r/r_{200}) \leq 0.2$.

It is also interesting to observe that M^* for the faint LF component gets brighter with increasing cluster-centric radius for the red galaxy population and fainter for the blue galaxies. We will fully discuss this feature in the context of color-selected giant and dwarf galaxies in Paper IV of this series.

4.3. Bright-End of the Luminosity Function
4.3.1. The Distribution of M^*

The variation in the value of M^* of the cluster LF can be used to gauge whether the LF is universal in shape at the bright-end, or whether luminosity segregation takes place (i.e., bright galaxies occupy preferentially the central regions of clusters). The measurement of M^* has been important, historically, for potential use as a "standard candle" (e.g., Schechter 1976; Dressler 1978; Colless 1989) and quantifying any variation in its value is important. We adopt the premise that the bright-end of the LF is universal if the median uncertainty of M^* is comparable to the measured dispersion of the distribution.

To measure the variation in the bright-end of the LF, the value of M^* was determined for our sample by fitting each cluster with a single Schechter function as described in §4.1; i.e., fitting the net galaxy counts in the magnitude range $-24 \leq M_{R_c} \leq -20$, with the faint-end slope fixed at $\alpha = -1$. Only galaxies measured within a cluster-centric radius of $(r/r_{200}) \leq 0.4$ were selected. This allows us to maximize the number of clusters in our sample while normalizing each one to the same dynamical radius without being adversely affected by small number statistics. Values for M^* for 55 clusters satisfying the magnitude and radius criteria are tabulated in Table 1.

In Figure 12 we plot the distribution of $M_{R_c}^*$, which appears approximately Gaussian with a mean $\langle M_{R_c}^* \rangle = -22.24 \pm 0.06$ and a dispersion of $\sigma = 0.31$ mag. The median uncertainty in the measurement of $M_{R_c}^*$ for all 55 clusters is 0.38 mag, thus supporting the universality of M^* within the measured range of $\Delta M^* \sim 0.3$ magnitude. Popesso et al. (2005) presents the histogram distribution of M^* for LFs measured within a radius of $2h_{50}^{-1}$ Mpc. Their distribution is Gaussian-like in shape with an estimated mean of ~ -22.6 and a dispersion of ~ 0.5 mag (transformed to our filter and distance scale). Given that the Popesso et al. LFs are measured with a fixed aperture, and at a larger radius than ours, it is not un-

expected that they obtain a somewhat larger dispersion and a brighter mean $M_{R_c}^*$ than our results, which may arise from a mild dependence of M^* on cluster-centric radius (see §4.3.2).

Given the size of the dispersion, our results are not too dissimilar even though Popesso et al. used a fixed physical length scale for the counting aperture size rather than scaling relative to a dynamical radius like r_{200}.

Since the uncertainty in $M_{R_c}^*$ is expected to be a function of cluster richness (assuming Poisson statistics), we measure the median uncertainty and dispersion of M^* for three bins based on cluster richness; i) $B_{gc} > 1500$, ii) $1000 < B_{gc} < 1500$, and iii) $B_{gc} < 1000$. The dividing B_{gc} values are equivalent to line-of-sight velocity dispersions of $\sigma_v \sim 960$ km s^{-1} for $B_{gc} = 1500$ and $\sigma_v \sim 750$ km s^{-1} for $B_{gc} = 1000$ (Yee & Ellingson 2003). For clusters with $B_{gc} > 1500$, we find a median uncertainty in $M_{R_c}^*$ of 0.22 mag with a corresponding dispersion of 0.25 mag. For the cluster sample with $1000 < B_{gc} < 1500$, we obtain a median uncertainty of 0.35 mag and a dispersion of 0.35 mag. Finally, for the poorest group we measure a median uncertainty of 0.51 mag and a dispersion of 0.32 mag. A comparison of the median uncertainty and dispersion of $M_{R_c}^*$ for our three cluster sub-samples supports the hypothesis that the bright-end of the cluster LF is universal at the ~ 0.3 mag level.

A direct comparison of $\langle M_{R_c}^* \rangle$ with other published values is problematic given that $M_{R_c}^*$ is not independent of α (Schechter 1976). Piranomonte et al. (2001) finds $M_r^* = -22.02 \pm 0.16$ for the combined LF from a sample of 80 clusters using a Schechter function fit with $\alpha = -1.01$. The composite LF for this study was constructed by weighting clusters according to their richness. Transforming M_r^* to the R_c passband (Fukugita et al. 1995) and our adopted cosmology, we find $M_{R_c}^* = -22.39 \pm 0.16$, which is in very good agreement with our result. From a sample of 69 clusters extracted from the RASS-SDSS, Popesso et al. (2006) found $M_r^* = -20.94 \pm 0.16$ and $\alpha = -1.09$. The cluster galaxies were measured within a cluster-centric radius of r_{200}. Transforming to our cosmology and passband yields $M_{R_c}^* = -22.64 \pm 0.16$, which is consistent with our measurement.

Hansen et al. (2005) presents M_r^* for a sample of clusters/groups selected from the SDSS Early Data Release. The Hansen et al. study tabulates M_r^* for several cluster samples of various richness with a faint-end slope fixed at $\alpha = -1.0$ (see their Table 2). The value of M^* for their richest sub-sample, which compares more directly with our Abell clusters, was determined to be $M_r^* = -20.86 \pm 0.05$. Transforming to our adopted cosmology and R_c-band filter, we find $M_{R_c}^* = -22.53 \pm 0.05$. This result is based on cluster galaxies measured within r_{200} and is in excellent agreement with our results. Hansen et al. also suggests that M^* is correlated with cluster richness in the sense that richer clusters have a brighter M_r^*. For their three richest bins, M_r^* differs by $\sim 4\sigma$ between the poorest and richest sub-samples. To search for a similar correlation in our Abell sample, we have divided our clusters into three bins based on B_{gc}; i) $B_{gc} < 1000$, ii) $1000 \leq B_{gc} < 1500$, and iii) $B_{gc} > 1500$. For these three sub-samples we find $M_{R_c}^* = (-22.36 \pm 0.08, -22.25 \pm 0.07, -22.28 \pm 0.05)$ for

$B_{gc} = (< 1000, 1000 - 1500, > 1500)$. No correlation between $M_{R_c}^*$ and cluster richness (as measured by B_{gc}) is evident.

To search for a possible correlation with richness for individual clusters, we plot in Figure 13 the distribution of $M_{R_c}^*$ as a function of B_{gc}. A Spearman rank-order correlation coefficient (Press et al. 1992) indicates that a correlation between $M_{R_c}^*$ and B_{gc} is not significant ($r_s = -0.08$), with a 45% probability that the variables are correlated. It is not too surprising that cluster richness, as measured by B_{gc}, does not have a strong influence on $M_{R_c}^*$ since we have normalized our cluster sample in terms of r_{200}. In Figure 13 we do see a trend where the spread in the measured value of $M_{R_c}^*$ decreases with increasing B_{gc}. This is most-likely due to the increased uncertainty in the measurement of $M_{R_c}^*$ for poorer clusters. For the ten clusters with the smallest value of B_{gc}, the average uncertainty in $M_{R_c}^*$ is 0.69 mag, while for the ten clusters with the largest value of B_{gc}, the mean uncertainty is 0.22 mag.

Hilton et al. (2005) finds a correlation between $M_{b_j}^*$ and X-ray luminosity such that low-L_X clusters have a brighter M^* than high-L_X systems ($\Delta M \sim 0.51$ mag). To compare our results, we use L_X measurements from Ebeling et al. (1996, 2000) for a sub-sample of 41 clusters in common and construct composite LFs for a low-L_X ($L_X < 3 \times 10^{44}$ ergs s^{-1}; 22 clusters) and a high-L_X sample ($L_X \geq 3 \times 10^{44}$ ergs s^{-1}; 19 clusters). Fitting a single Schechter function to the LFs yields $M_{R_c}^* = -22.25 \pm 0.06$ for the low-L_X sample and $M_{R_c}^* = -22.22 \pm 0.05$ for the high-L_X group. Thus, there is no significant difference in M^* when dividing our sample in terms of L_X. The discrepancy between our result and Hilton et al. may be due to the higher fraction of low-mass systems in their sample. For example, using the same dividing L_X as Hilton et al. (0.36×10^{44} erg s^{-1}), our low-L_X sample contains only 3 clusters (7% of the total), while the corresponding Hilton et al. sample contains 49 clusters (72% of the total).

To search for a correlation of LF parameters with cluster mass, De Propris et al. (2003) divided their sample into two groups based on velocity dispersion ($\sigma \gtrsim 800$ km s^{-1}). A Schechter function fit to the low- and high-σ group yields the same M^* at the 1σ level. This is consistent with our findings that M^* is not correlated with cluster mass.

The characterization of clusters based on the relative contrast of the brightest cluster galaxy defines the Bautz-Morgan type (BM-type) classification scheme (Bautz & Morgan 1970). The evolutionary state of a cluster, as characterized by its BM-type, is expected to be correlated with M^* if the BCGs are created via the merger of giant galaxies through a cannibalism-like process (e.g., Dressler 1978). Galactic cannibalism would reduce the number of bright galaxies and therefore shift $M_{R_c}^*$ to a fainter value. To test this scenario, we plot in Figure 14 M^* versus BM-type for 54 clusters (A1569 has no published BM-type). The solid line in Figure 14 depicts a least-squares fit to the data and suggests that a weak correlation exits in the sense that early BM-type clusters have a fainter M^* than later BM-types. A Spearman rank-order test gives a correlation coefficient of $r_s = -0.28$, with a 96% probability that these two variables are correlated. This result lends support to the theoretical study of Merritt (1984) in which the formation of the BCG occurs while the cluster is collapsing. It is expected that relatively little evolution of the BCG happens after the cluster is virialized. If we associate the early BM-type clusters with fully relaxed virialized systems and late BM-types with unrelaxed systems in the process of collapsing, the trend of the correlation between M^* and BM-type from Figure 14 can be explained.

Since M^* is correlated with BM-type, we correct the values of M^* for this correlation and find that the dispersion in $M_{R_c}^*$ decreases from 0.31 mag to 0.24 mag. This result is consistent with the universality of M^* within the 0.3 mag range.

To investigate the possible correlation between M^* and B_{gc} for selected BM-types, we divide our 54 clusters into early BM-types (I and I-II) and late BM-types (II, II-III, and III). A Spearman rank-order correlation analysis for the early BM-type sample yields $r_s = -0.27$, with a 72% probability that M^* and B_{gc} are correlated. For the late BM-type clusters we find $r_s = -0.08$ with only a 39% probability that M^* and B_{gc} are correlated. These results indicate that no significant correlation exists between M^* and cluster richness among similar BM-type clusters when measuring galaxies within an equivalent dynamical radius and thus further supports the notion that M^* is universal within the measured uncertainty.

De Propris et al. (2003) compares their composite LF fit parameters for two sub-samples divided according to BM-type. The difference in M^* between the early BM-type group (I, II-II, II) and the late BM-type sample (II-III, III) is 0.06 ± 0.22 mag, where the uncertainties in M^* are added in quadrature. The difference in M^* between our BM-type I and III systems is $\Delta M = 0.3$ mag, which is significant at the 3σ level. Using identical BM-type bins as De Propris et al., we find $\Delta M = 0.2$ mag at the 3σ level. The discrepancy between our result and De Propris et al. may be related to differences in the technique used to construct the composite LFs. For example, De Propris et al. includes the BCG in their LFs. In addition, instead of using a dynamically scaled radius, De Propis et al. used all galaxies within a fixed aperture of $1.5h_{100}^{-1}$ Mpc, which may add to the dispersion of M^*. Also, galaxy magnitudes from De Propris et al. are based on m_{b_j} magnitudes, which are more susceptible to recent star formation and dust attenuation than R_c magnitudes. In addition, De Propris et al. fits for the value of α while we impose the constraint that $\alpha = -1$. Since M^* and α are correlated, a steeper α will in general yield a fainter M^*. The faint-end slope of the early BM-type LF from De Propris et al. is flatter than the slope of the late BM-type LF. Forcing α to be the same will increase ΔM between these two samples. Although the difference in M^* between the BM-type samples in De Propris et al. is not significant, it is interesting to note that the late BM-type sample has a slightly brighter M^*, equivalent to the trend we measure.

4.3.2. The Cluster-Centric Radial Dependence of M^*

The variation of M^* as a function of cluster-centric radius was examined by measuring the bright-end of the composite LF constructed from our entire 57 cluster sample. These clusters are 100% photometrically complete to $M_{R_c} = -20$, and thus maximize the number of clusters

used to determine M^* in order to minimize its measured uncertainty. (Recall that the M^* values tabulated in Tables 2–4 are measured for a sample of 42 clusters that are complete to $M_{R_c} = -16.5$.)

The dependence of M^* on cluster-centric radius was determined by fitting a single Schechter function to the net galaxy counts from $-24 \leq M_{R_c} \leq -20$ for the four radial bins used previously (for example, see Figure 3). The faint-end slope of the Schechter function was fixed at $\alpha = -1.0$ as was done when measuring M^* for the individual cluster LFs. Since different clusters cover various fractions of r_{200}, the total number of clusters contributing to the composite sample will vary with cluster-centric radius.

In Figure 15 we plot M^* as a function of (r/r_{200}) for the total composite cluster sample, as well as samples compiled by selecting red and blue galaxies from our 57-cluster sample (see §4.2 for color selection criteria). Inspection of Figure 15 reveals that for the red and blue composite samples, M^* gets brighter with increasing cluster-centric radius. For the total composite sample, we find a similar correlation, although the trend is much weaker. This weaker trend is due to the interplay between the relative dominance of the red and blue galaxies as a function of cluster-centric radius. M^* near the center is dominated by red galaxies; whereas at larger radii, blue galaxies with a fainter M_{R_c} become an increasingly more important component, flattening the $M_{R_c}^*$ dependence on radius. The difference in M^* between the inner- and outer-most radial bin is $\Delta M = 0.48$ mag for the red sequence LF (3.3σ level) and $\Delta M = 0.27$ mag for the blue LF (1.2σ level).

To quantify the correlation for each of our three composite cluster samples, we calculate the linear correlation coefficient r statistic (Press et al. 1992). For the total composite cluster sample, we find that the linear correlation coefficient is $r = -0.91$, with a 92% probability that M^* and radius are correlated. The red sequence composite cluster sample yields $r = -0.98$, with a 98% probability of a correlation. For the blue galaxy cluster sample, the linear correlation coefficient is $r = -0.98$ and a 98% probability of a correlation.

5. DISCUSSION AND CONCLUSIONS

5.1. *Universality of the Luminosity Function*

We have examined the distribution of M^* for the bright-end of the LF in the core of Abell clusters. We found that the dispersion in M^* is comparable to the average measured uncertainty, even when dividing the cluster sample into different richness groups based on B_{gc}. We use this result to indicate that M^* is universal at the 0.3 mag level for a restricted magnitude range and when measured within a specific dynamical radius. In addition, we find a weak trend in which early BM-type clusters have a fainter M^* than late BM-types.

One of the primary goals of this paper is to explore the change in the cluster R_c-band LF as a function of cluster-centric radius. From a sample of 57 low-z Abell clusters, we have measured LFs covering various fractions of r_{200} for both the red sequence and blue cluster galaxy populations. Our results indicate that the overall shape of the LF is dependent upon distance from the cluster center. In general, the LFs exhibit an increase in the steepness of the faint-end slope with increasing ra-

dius. The radial dependence of the rate-of-change in α is greatest for the total cluster sample (i.e., red plus blue galaxies), while the blue LF is less dependent. The red sequence LF is mostly flat ($\alpha \sim -1$) over a span of ~ 5 magnitudes ($-23 < M_{R_c} < -18$), with a rising faint-end for $M_{R_c} > -18$. In contrast, the blue galaxy LF is much steeper ($\alpha \sim -1.8$) over this same luminosity range, with minimal change in shape out to r_{200}. The very rapid increase in α for the total LF is likely due to a combination of steepening slope for both red and blue LFs and the increasing dominance of the blue population at large cluster-centric radii. In addition, the red sequence LF has a much brighter characteristic magnitude (~ 0.6 mag) over all radii than the blue galaxy luminosity distribution. These results lend support to several recent studies that have observed similar characteristics for red and blue galaxy LFs drawn from low- to high-density environments (e.g., Beijersbergen et al. 2002a; Goto et al. 2002; Baldry et al. 2004).

The general trend for the LF to become flatter with decreasing cluster-centric radius supports the hypothesis that dwarf galaxies are tidally disrupted near the cluster center. This idea has been used by López-Cruz et al. (1997) to help explain the formation of BCG halos and the origin of a large fraction of the gas content in the intracluster medium.

The dependence of the shape of the LF on cluster-centric radius provides strong evidence that the relative mixture of giant and dwarf galaxies depends on the fraction of the virial radius that is measured. This argues against the global universality of the cluster LF for the magnitude interval $-26 \leq M_{R_c} \leq -16.5$ and suggests an environmental influence. The non-parametric galaxy dwarf-to-giant ratio will be explored in Paper IV of this series.

In Figure 16 we plot composite cluster LFs from several published sources (Colless 1989; Piranomonte et al. 2001; Goto et al. 2002; De Propris et al. 2003; Hansen et al. 2005; Popesso et al. 2006). These LFs have been transformed to M_{R_c} using Fukugita et al. (1995) and our adopted cosmology. Also depicted in Figure 16 are the total composite LFs from this study for the inner- and outer-most radial bin. In addition, the SDSS field galaxy LF from Blanton et al. (2003) is included for comparison purposes.

Figure 16 illustrates that the slope of the LFs are very similar at bright magnitudes where the giant galaxies have the greatest influence on the shape of the LF. The main difference in the slope arises at the faint-end where the influence of the dwarf galaxies tends to increase the steepness of α. The sampling depth and effective cluster-centric radius thus has a major influence on the measured shape of the cluster LF since the inclusion of different amounts of the dwarf galaxy population will directly impact the faint-end slope. Thus, the evidence supports the notion that the cluster LF is not universal in shape in a global sense. In addition, we measure a dispersion of 0.3 mag in the value of M^* for the depicted cluster LFs; the faintest value is $M_{R_c}^* = -22.26$ for the inner-most annuli from this study and the brightest is $M_{R_c}^* = -23.14$ from Goto et al. (2002).

5.2. *Cluster Galaxy Population Gradients*

As discussed in §4.3.2, Figure 15 shows that the bright-end M^* becomes brighter with increasing cluster-centric radius for both the red, and with a lesser significance, the blue cluster galaxies. The observed dimming of M^* toward the cluster center can be explained as a simple fading of the galaxy population. For the blue cluster galaxies, the truncation of star formation as field galaxies fall into the cluster environment (e.g., Abraham et al. 1996; Ellingson 2003) would lead to a fading of M^* with decreasing cluster-centric radius. Since clusters are believed to have formed via the infall of galaxies along filamentary-like structures (e.g., Dubinski 1998), it is expected that a population of infalling field galaxies can be detected in addition to the older, mainly early-type red galaxies. If star formation for infalling spiral galaxies, which dominate the field galaxy population (e.g., Binggeli et al. 1988), is truncated via some type of dynamical mechanism (e.g., ram pressure stripping, galaxy harassment, etc.; Moore et al. 1998; Goto 2005; Roediger et al. 2006), then a roughly continuous infall (but with an allowed variable rate) would be observed as a fading of the population toward the cluster center. Given enough time, infalling spiral galaxies may acquire characteristics that are similar to S0 galaxies. In fact, this type of mechanism for S0 formation has been proposed by numerous authors (see Dressler et al. 1999, and references therein), although the formation of field S0s has remained problematic for these models.

The dimming of M_2^*, or the decrease of (N_2^*/N_1^*) for the faint-end of the red sequence LF for decreasing cluster-centric radii, places constraints on the evolutionary path of the faint blue galaxies. If these galaxies simply fade and turn red, we would expect them to contribute to the red sequence LF by increasing the number of faint red galaxies in the central cluster region. We thus suggest that the faint blue cluster galaxies are destroyed in the central cluster region. This is not a far-fetched hypothesis since the faint blue galaxies are very similar to the low-mass dwarf spheroidal galaxies, which are expected to undergo tidal disruption in the central cluster environment (Thompson & Gregory 1993; Gallagher & Wyse 1994; Hilker et al. 2003). These low luminosity blue galaxies could also be the source of the dwarf galaxies that get tidally disrupted and form the halo of BCGs as proposed in a model by López-Cruz et al. (1997). We will explore this possibility further in Paper IV of this series.

The fading of the bright-end M^* for the red sequence galaxy population may be the result of two separate processes; the continuous fading of infalling red galaxies (which may have turned red relatively recently due to the truncation of star formation) and galactic cannibalism in the high-density central cluster region. For the infall scenario, red galaxies are expected to originate from a population that had arrived in the cluster environment early in its history. The observed dispersion of the CMR for the cluster red sequence places constraints both on the formation timescale of the early-type galaxy population (i.e., $z > 2$; e.g., Stanford et al. 1998; De Propris et al. 2004; Gladders et al. 1999; Holden et al. 2004; López-Cruz et al. 2004) and any episodes of recent star formation (e.g., Bower et al. 1998). Red galaxies which have entered the cluster environment during the earliest part of the cluster lifetime, would be expected to be the faintest since the time between the last phase of major star formation and today would be the greatest for these galaxies (after the truncation of star formation, galaxies would evolve passively with an associated reddening and dimming of their starlight). Under this scenario, we would expect that the blue galaxy population would show a greater rate-of-change in M^* with radius due to the more recent decline in the star formation rate. The red galaxies would be expected to exhibit a more gradual change in M^*, as compared to the blue galaxy population, since the red galaxies are just a passively evolving old galaxy population.

As depicted in Figure 15 the bright-end M^* for the red sequence galaxies fades more rapidly toward the cluster center than for the blue galaxy population. Since a simple infall scenario as described predicts that the blue galaxy population should exhibit the more rapid decline in M^*, we hypothesize that an additional mechanism may affect the rate-of-change of M^* with radius for the red galaxy population. A clue to this additional effect is gleamed from Figure 14 where the correlation between M^* and BM-type is depicted for the total cluster sample. As described in §4.3.1, the trend for a brightening of M^* with later BM-type can be explained by galactic cannibalism. As first theorized by Ostriker & Hausman (1977) and Hausman & Ostriker (1978), as bright galaxies fall into the cluster center they will be swallowed by the giant central galaxy, thus resulting in the fading of M^* as bright galaxies are depleted from the LF. Since early BM-type clusters have, by definition, a bright central dominant galaxy, the correlation depicted in Figure 15 is expected. Galactic cannibalism will also result in the fading of M^* with decreasing cluster-centric radius, as illustrated in Figure 15. We performed a simple test of this hypothesis by calculating M^* for our red cluster galaxy sample for early BM-type clusters (I and I-II) and late BM-type clusters (II, II-III, and III). We assume that the effect of galactic cannibalism on the radial dependence of M^* will be greatest for the early BM-type sample. Comparing M^* between the inner- and outer-most radial bin shows that for the early BM-type sample, $\Delta M = 0.71$ mag with the two measurements different at the 2σ level. For the late BM-type sample, we find $\Delta M = 0.36$ mag at the 2σ level. Although the significance of the difference in M^* for a given BM-type group is not high (partly due to the fact that only four clusters comprise the outer-most radial bin for the early BM-type clusters), the larger difference in M^* for the early BM-type sample suggests that the infall and galactic cannibalism scenarios may help to explain the observed rate-of-change of M^* with radius for the red sequence galaxy population.

In Paper IV of this series we will further elucidate the nature of the cluster galaxy population by examining the radial-dependence of the dwarf-to-giant ratio and the blue-to-red galaxy count ratio. These results will complement the observations presented in this paper and provide additional constraints on the composition of the galaxy population in low-redshift Abell clusters.

APPENDIX

A. QUANTIFYING SELECTION EFFECTS AND BIASES

A major challenge when conducting any observational study is the ability to quantify the impact of selection effects and biases on the robustness of the results. In this appendix we explore several of these potential sources of systematic errors and quantify their affect on the derived galaxy cluster LF.

A.1. *Chance Projections*

A main concern in interpreting the results of a study based on the LF constructed from the statistical subtraction of background galaxies is the possible influence of projection effects. The chance projection of field galaxies, or unrelated groups, can appear as clusters when redshift information is not available (Valotto et al. 2001). Selection of cluster members using color information (see §3.2) helps to alleviate some of this concern. To determine what impact chance projections may have on our LFs, we have divided our cluster sample into two groups according to the number of published redshifts (e.g., Struble & Rood 1999). The first group contains only those clusters which have at least 25 spectroscopically-confirmed cluster members. The second group contains clusters in which the number of redshift-confirmed members is ≤ 10. In this comparison it is assumed that clusters with a small number of confirmed members may still suffer from unknown projection effects.

In Figure 17 we present LFs for the total composite cluster sample for four different radial bins. The cluster sample has been divided into two groups according to the number of confirmed cluster members based on the number of redshifts (i.e., 20 clusters with ≤ 10 galaxy redshifts and 32 clusters with ≥ 25 galaxy redshifts). The LFs for each radial bin have been scaled to match the LF for that particular cluster-centric radius from the total composite LFs depicted in Figure 3. The overall shape of the LFs generated for the two redshift-selected cluster groups are very similar in shape for all four annuli. Hence, this test indicates that the chance projection of background clusters/galaxy groups does not have a significant effect on our results.

A.2. *Deprojecting the Luminosity Function*

The LFs presented in this paper are derived from the two-dimensional projected distribution of cluster galaxies. Since the full three-dimensional galaxy spatial positions cannot be resolved, the presence of contaminating galaxies from *within* the cluster can adversely affect the accuracy in determining the shape of the central cluster LF. Note that in this context, the projected galaxies are those which lie in the outskirts of the cluster and are projected onto the central region. This is in addition to the presence of fore/background galaxies that are unrelated to the target cluster, and are corrected using background corrections. The projection of galaxies located in the outskirts of clusters onto the central region will have its greatest impact on the faint-end of the central LF. This is due to the increase in the relative fraction of dwarf galaxies with increasing cluster-centric radius, as implied by the steepening of the faint-end slope with radius (see Figure 3).

Simulations by Valotto et al. (2001) indicate that projection effects can severely affect the shape of the LF by artificially producing a steeper faint-end slope. Some of this steepening is due to the fact that cluster galaxies were not selected in terms of color (i.e., using the CMR), thus resulting in contamination by projected field galaxies. A certain portion can also be attributed to the inclusion of galaxies in cluster outskirts that are projected onto the central region. Beijersbergen et al. (2002a) published a study of the LF of the Coma cluster in which they corrected the LF for projection effects by subtracting the contribution of the outer Coma LF that is projected onto the central region. The resulting "deprojected" LF was measured to be marginally flatter than the projected 2-d LF.

To determine the extent to which our LFs are affected by projection effects from the galaxy population in the cluster outskirts, we have measured the deprojected composite LF for the total, red sequence, and blue galaxy samples. We assume that the cluster galaxies are distributed symmetrically in a sphere about the cluster center with the method of deprojecting the LF depicted in Figure 18. As shown, any sight-line to the central area of the cluster (region A) must pass through regions B1 and B2. Thus, the observed central LF will include galaxies that are located in regions B1 and B2. To correct for this effect, the LF determined from region C is subtracted from the LF calculated for the regions B1+B2+A. Before subtracting the two LFs, the LF measured for region C must be normalized to the same volume as that included in regions B1+B2. This "correction" factor is given by $(V_1 - V_2)/(V_3 - V_1)$, where V_1 is the

combined volume of regions B1+B2+A, V_2 is the volume of the inner region A ($V_2 = (4\pi/3)R_1^3$), and V_3 is the volume of the outer-most sphere ($V_3 = (4\pi/3)R_2^3$). The volume V_1 can be calculated from $V_1 = (4\pi/3)\left[R_2^3 - (R_2^2 - R_1^2)^{3/2}\right]$, where R_1 is the radius of the inner sphere, and R_2 is the radius of the outer sphere.

Using this procedure, the deprojected composite LF for the total, red sequence, and blue galaxy samples were constructed for two radial bins, $(r/r_{200}) \leq 0.2$ and $0.2 \leq (r/r_{200}) \leq 0.4$. The large uncertainty in the net galaxy counts from the deprojection process limits our analysis of the LF to these two inner-most radial bins. In Figures $19-21$ comparisons between the projected and deprojected LFs for the three cluster galaxy samples are presented. For each figure the LFs have been scaled to match in the $-22 \leq M_{R_c} \leq -21$ magnitude range to facilitate the comparison. The top panel for each of the three figures depicts the deprojected LF for the two inner-most radial bins. For all three galaxy samples, the LF for the $(r/r_{200}) \leq 0.2$ radial bin (open triangles) has a flatter faint-end slope than for the $0.2 \leq (r/r_{200}) \leq 0.4$ radial bin (solid triangles). Thus, the trend of a steepening faint-end slope with increasing cluster-centric radius is valid for the deprojected LFs for the total, red sequence, and blue galaxy samples.

In the middle panel of Figures $19-21$, the deprojected and projected LFs are compared for the $(r/r_{200}) \leq 0.2$ radial bin. For all three galaxy samples, the deprojected LF has a flatter faint-end slope than the projected LF. This demonstrates that galaxies from the cluster outskirts that are projected onto the central cluster region will result in an artificial steepening of the faint-end of the central LF.

The bottom panel of Figures $19-21$ presents the deprojected and projected LFs for the $0.2 \leq (r/r_{200}) \leq 0.4$ radial bin. In general, the shape of the LFs are very similar given the size of the uncertainties in the net galaxy counts. No statistically significant difference in the shape of the deprojected and projected LFs can be discerned for either the total, red sequence, or blue galaxy cluster samples.

The deprojection of the cluster LF indicates that the presence of galaxies from the outer cluster region can affect the slope of the faint-end, especially for the central region. The basic trend of a steepening faint-end slope with increasing cluster-centric radius is still evident from the deprojected LF data.

A.3. Faint Source Correction

The shape of the faint-end of the cluster LF can be affected by bias as a result of counting galaxies in the faintest magnitude bin. The faint galaxy correction (also known as the Eddington bias or correction; Eddington 1940) is due to the fact that each observed galaxy has an associated magnitude uncertainty, causing galaxies to be scattered below and above our observed magnitude limit. If the number distribution of galaxies is identical over all magnitudes, the number of galaxies scattered above and below our magnitude threshold will be statistically equal. A cluster LF having a faint-end slope steeper than $\alpha = -1$, will have a net number of galaxies scattered brighter than the observed magnitude limit. This will artificially enhance the number of detected galaxies at the faint-end of the LF. Since our galaxy counts are binned to produce the LF, the magnitude bin size relative to the uncertainty of the measured galaxy magnitudes will have a direct impact on the importance of this bias.

To investigate the impact of the faint source correction on our measured LFs, simulated LFs using the shape parameters tabulated in Table 2 for the total composite LF were constructed. For each galaxy magnitude we include an offset calculated from the observed distribution of magnitude uncertainty σ_{R_c} as a function of M_{R_c}, assuming Gaussian statistics. The magnitude offset applied to each simulated galaxy was randomly chosen from a Gaussian distribution with a dispersion of $1\sigma_{R_c}$. Simulated LFs were assembled using the same selection criteria as that used for the observed LFs. The fractional change in the number of galaxies detected in the faintest magnitude bin $(-17.0 \leq M_{R_c} \leq -16.5)$ depends directly on the value of α_2. Comparing simulated LFs to those tabulated in Table 2 yields an increase from 0.0% to $+0.4\%$ in the number of detected galaxies in the faintest magnitude bin as the value of α_2 changed from -1.18 to -2.43. This demonstrates that the increase in the number of detected galaxies due to the scattering of faint galaxies into the faintest magnitude bin, is insignificant given the measured range in α_2. This result is reasonable given the relatively large width of our magnitude bins (0.5 mag) and the average magnitude uncertainty (~ 0.1 mag) at our imposed faint-end magnitude limit.

A.4. Color Selection Bias

The study of the LF of galaxies selected according to their position in the color-magnitude plane could be affected by a color bias. This bias is a result of scattering in $B - R_c$ and R_c of galaxies due to photometric uncertainties. To understand the extent of this effect, an artificial galaxy catalog for Abell 260 was constructed by taking the original galaxy catalog and adding a small, random magnitude offset based on the measured R_c magnitude and its uncertainty for each galaxy, assuming Gaussian statistics. By tracking the relative offset in position on the CMD between the original cluster galaxies and their simulated counterparts, the impact of the color bias can be measured.

In Figure 22 a vector-type CMD for Abell 260 is presented for galaxies brighter than the cluster completeness limit ($R_c = 20.7$). The vectors trace the scattering path of a galaxy from its initial position in the observed color-magnitude plane to its position in the artificial catalog. For bright galaxies, the change in position is minimal compared to the size of the region from where the galaxies are selected (see Figures 5 and 8 for selection of red sequence and blue galaxies). The largest displacement in the color-magnitude plane occurs for the faint red galaxies where the relatively large uncertainties in $B - R_c$ produce a larger change in color. The magnitude of this displacement is not significant compared to the size of the regions used to select red and blue galaxies. This exercise justifies the method used to select faint red sequence galaxies (see §4.2.2, criterion 2). By restricting the selection of faint red sequence galaxies from a region redward of the CMR (see Figure 5), the contamination from blue galaxies scattered into the red sequence region is minimized.

A.5. *Dynamical Radius Variation*

As stated in Section 3.4, the value of r_{200} determined from B_{gc} (via equation 7) has an associated rms scatter of $\sim 15\%$. To determine whether a 15% scatter in r_{200} will have a significant influence on our conclusions, a simulated composite LF was derived by randomly changing r_{200} by $\pm 15\%$. A comparison of the observed LF with the simulated LF is presented in Figure 23 for the four cluster-centric radial bins used previously. Inspection of Figure 23 shows that the two LFs are equivalent for each radial bin depicted. Thus, the 15% scatter in the value of r_{200} is expected to have minimal impact on our results. This is at least in part due to the expected gradual change in the properties of the LF as a function of r_{200}.

A.6. *Exclusion of the Brightest Cluster Galaxy*

In §4.1 it was noted that the BCG was not included in the construction of the cluster LF since they do not appear, statistically, to be a natural extension of the LF. In Figure 24 the composite LF for the inner-most radial bin, $(r/r_{200}) \leq 0.2$, is depicted for clusters (complete to $M_{R_c} = -20$) with and without the inclusion of the BCG. As this figure demonstrates, the BCGs are not a simple extension of the Schechter function, which may indicate that BCGs are formed by a different process (e.g., mergers, cannibalism, etc.; Dressler 1978) than the fainter cluster galaxy population.

REFERENCES

Abell, G. O. 1962, in IAU Symp. 15, Problems of Extra-Galactic Research, ed. G. C. McVittie (New York: Macmillan Press), 213
Abraham, R. G., et al. 1996, ApJ, 471, 694
Akritas, M. G., & Bershady, M. 1996, ApJ, 470, 706
Akritas, M. G., & Siebert, J. 1996, MNRAS, 278, 919
Andreon, S., Willis, J., Quintana, H., Valtchanov, I., Pierre, M., & Pacaud, F. 2004, MNRAS, 353, 353
Aguerri, J. A. L., Sánchez-Janssen, R., & Muñoz-Tuñón, C. 2007, preprint (astro-ph/0704.1579)
Baldry, I. K., Glazebrook, K., Brinkmann, J. Ivezić, Ž., Lupton, R. H., Nichol, R. C., & Szalay, A. S. 2004, ApJ, 600, 681
Barkhouse, W. A. 2003, Ph.D. thesis, Univ. Toronto
Bautz, L. P., & Morgan, W. W. 1971, ApJ, 162, L149
Beijersbergen, M., Hoekstra, H., van Dokkum, P. G., & van der Hulst, T. 2002a, MNRAS, 329, 385
Beijersbergen, M., Schaap, W. E., & van der Hulst, J. M. 2002, A&A, 390, 817
Bernstein, J. P., & Bhavsar, S. P. 2001, MNRAS, 322, 625
Bhavsar, S. P. 1989, ApJ, 338, 718
Binggeli, B., Sandage, A., & Tammann, G. A. 1988, ARA&A, 26, 509
Biviano, A., Durret, F., Gerbal, D., Le Févre, O., Lobo, C., Mazure, A., & Slezak, E. 1995, A&A, 297, 610
Blanton, M. R., et al. 2003, ApJ, 592, 819
Bower, R. G., Kodama, T., Terlevich, A. 1998, MNRAS, 299, 1193
Brown, J. P. 1997, Ph.D. thesis, Univ. Toronto
Burstein, D., & Heiles, C. 1982, AJ, 87, 1165
Burstein, D., & Heiles, C. 1984, ApJS, 54, 33
Carlberg, R. G., Yee, H. K. C., & Ellingson, E. 1997, ApJ, 478, 462
Christlein, D., & Zabludoff, A. I. 2003, ApJ, 591, 764
Cole, S., & Lacey, C. 1996, MNRAS, 281, 716
Coleman, G. D., Wu, C. C., & Weedman, D. W. 1980, ApJS, 43, 393
Colless, M. 1989, MNRAS, 237, 799
De Propris, R., et al. 2003, MNRAS, 342, 725
De Propris, R., Stanford, S. A., Eisenhardt, P. R., Dickinson, M., & Elston, R. 2004, AJ, 118, 719
Dressler, A. 1978, ApJ, 223, 765
Dressler, A. 1980, ApJ, 236, 351
Dressler, A., Smail, I., Poggianti, B. M., Butcher, H., Couch, W. J., Ellis, R. S., & Oemler, A. 1999, ApJS, 122, 52
Driver, S. P., Phillipps, S., Davies, J. I., Morgan, I., & Disney, M. J. 1994, MNRAS, 268, 393
Driver, S. P., Couch, W. J., & Phillipps, S. 1998, MNRAS, 301, 369
Dubinski, J. 1998, ApJ, 502, 141
Ebeling, H., Voges, W., Böhringer, H., Edges, A. C., Huchra, J. P., & Briel, U. G. 1996, MNRAS, 281, 799
Ebeling, H., Edges, A. C., Allen, S. W., Crawford, C. S., Fabian, A. C., & Huchra, J. P. 2000, MNRAS, 318, 333
Eddington, A. S. 1940, MNRAS, 100, 354
Ellingson, E., Lin, H., Yee, H. K. C., & Carlberg, R. G. 2001, ApJ, 547, 609
Ellingson, E. 2003, Ap&SS, 285, 9
Ferguson, H. C., & Binggeli, B. 1994, A&A Rev., 6, 67
Frei, Z., & Gunn, J. E. 1994, AJ, 108, 1476
Fukugita, M., Shimasaku, K., & Ichikawa, T. 1995, PASP, 107, 945
Gaidos, E. J. 1997, AJ, 113, 117
Gallagher, J. S., & Wyse, R. F. G. 1994, PASP, 106, 1225
Garilli, B., Maccagni, D., & Andreon, S. 1999, A&A, 342, 408
Geller, M. J., & Peebles, P. J. E. 1976, ApJ, 206, 939
Gladders, M. J., López-Cruz, O., Yee, H. K. C., & Kodama, T. 1999, ApJ, 501, 571
Godwin, J. G., & Peach, J. V. 1977, MNRAS, 181, 323
González, R. E., Lares, M., Lambas, D. G., & Valotto, C. 2006, A&A, 445, 51
Goto, T. 2005, MNRAS, 359, 1415
Goto, T., et al. 2002, PASJ, 54, 515
Goto, T., et al. 2005, ApJ, 621, 188

Hansen, S. M., McKay, T. A., Wechsler, R. H., Annis, J., Sheldon, E. S., & Kimball, A. 2005, ApJ, 633, 122
Hausman, M. A., & Ostriker, J. P. 1978, ApJ, 224, 320
Hilker, M., Mieske, S., & Infante, L. 2003, A&A, 397, L9
Hilton, M., et al. 2005, MNRAS, 363, 661
Holden, B. P., Stanford, S. A., Eisenhardt, P., & Dickinson, M. 2004, AJ, 127, 2484
Hubble, E. P. 1936, ApJ, 84, 158
Humason, M. L., Mayall, N. U., & Sandage, A. R. 1956, AJ, 61, 97
Jones, C., & Forman, W. 1999, ApJ, 511, 65
Landolt, A. U. 1992, AJ, 104, 372
Loh, Y. -S., & Strauss, M. A. 2006, MNRAS, 366, 373
López-Cruz O. 1997, Ph.D. thesis Univ. Toronto
López-Cruz, O. 2001, Rev. Mex. AA Conf. Ser., 11, 183
López-Cruz, O., Yee, H. K. C., Brown, J. P., Jones. C., & Forman, W. 1997, ApJ, 475, L97
López-Cruz, O., Barkhouse, W. A., & Yee, H. K. C. 2004, ApJ, 614, 679
Lugger, P. M. 1986, ApJ, 303, 535
Madgwick,D. S. et al. 2002, MNRAS, 333, 133
Mercurio, A., Massarotti, M., Merluzzi, P., Girardi, M., La Barbera, F., & Busarello, G. 2003, A&A, 408, 57
Merritt, D. 1984, ApJ, 276, 26
Miller, C. J., et al. 2005, AJ, 130, 968
Molinari, E., Chincarini, G., Moretti, A., & De Grandi, S. 1998, A&A, 338, 874
Moore, B, Lake, G., & Katz, N. 1998, ApJ, 495, 139
Näslund, M., Fransson, C., & Huldtgren, M. 2000, A&A, 356, 435
Oemler, A. 1974, ApJ, 194, 1
Oke, J. B., & Sandage, A. 1968, ApJ, 154, 21
Ostriker, J. P., & Hausman, M. A. 1977, ApJ, 217, 125
Parolin, I., Molinari, E., & Chincarini, G. 2003, A&A, 407, 823
Piranomonte, S., Longo, G., Andreon, S., Puddu, E., Paolillo, M., Scaramella, R., Gal, R., & Djorgovski, S. G. 2001, in ASP Conf. Ser. 225, Virtual Observatories of the Future, ed. R. J. Brunner, S. G. Djorgovski, & A. S. Szalay (San Francisco: ASP), 73
Popesso, P., Böhringer, H., Romaniello, M., & Voges, W. 2005, A&A, 433, 415
Popesso, P., Biviano, A., Böhringer, H., & Romaniello, M. 2006, A&A, 445, 29
Popesso, P., Biviano, A., Böhringer, H., & Romaniello, M. 2007, A&A, 461, 397
Press, W. H., & Schechter, P. 1974, ApJ, 187, 425
Press, W. H., Teukolsky, S. A., Vetterling, W. T., & Flannery, B. P. 1992, Numerical Recipes, The Art of Scientific Computing, (2d ed.; Cambridge: Cambridge University Press)
Rines, K., Geller, M. J., Kurtz, M. J., & Diaferio, A. 2003, ApJ, 126, 2152
Roediger, E., Brüggen, M., & Hoeft, M. 2006, MNRAS, 371, 609
Sandage, A. 1976, ApJ, 205, 6
Schechter, P. 1976, ApJ, 203, 297
Spergel, D. N., et al., 2003, ApJS, 148, 175
Stanford, S. A., Eisenhardt, P. R., & Dickinson, M. 1998, ApJ, 492, 461
Struble, M. F., & Rood, H. J. 1999, ApJ, 125, 35
Thompson, L. A., & Gregory, S. A. 1993, AJ, 106, 2197
Trentham, N., Tully, R. B., & Verheijen, M. A. W. 2001, MNRAS, 325, 385
Valotto, C. A., Moore, B., & Lambas, D. G. 2001, ApJ, 546, 157
Yagi, M., Kashikawa, N., Sekiguchi, M., Doi, M., Yasuda, N., Shimasaku, K., & Okamura, S. 2002, AJ, 123, 87
Yang, Y., Zhou, X., Yuan, Q., Jiang, Z., Ma, J., Wu, H., & Chen, J. 2004, ApJ, 600, 141
Yee, H. K. C. 1991, PASP, 103, 396
Yee, H. K. C., Ellingson, E., & Carlberg, R. G. 1996, ApJS, 102, 269
Yee, H. K. C., & López-Cruz, O. 1999, AJ, 117, 1985
Yee, H. K. C. & Ellingson, E. 2003, ApJ, 585, 215

TABLE 1
CLUSTER PROPERTIES

Cluster	Redshift	$M_{R_c}^*$	$\Delta M_{R_c}^*$	B_{gc} (Mpc$^{1.8}$)	ΔB_{gc}	r_{200} (Mpc)	Δr_{200}	$M_{R_c}^{Com}$
A21	0.0946	−22.28	0.29	1480	229	2.641	0.396	−17.5[a]
A84	0.1030	−22.46	0.38	917	184	2.098	0.315	−17.5
A85	0.0518	−22.34	0.42	780	168	1.942	0.291	−16.0
A98	0.1043	−22.37	0.24	1657	243	2.788	0.418	−18.0
A154	0.0638	−22.11	0.32	1462	227	2.626	0.394	−16.5
A168	0.0452	−22.56	0.41	992	187	2.179	0.327	−16.0
A260	0.0363	−22.04	0.44	855	176	2.029	0.304	−16.0
A399	0.0715	−21.87	0.26	1427	224	2.595	0.389	−17.5
A401	0.0748	−22.25	0.19	2242	279	3.224	0.484	−17.0
A407	0.0472	−22.39	0.37	1327	216	2.506	0.376	−16.5
A415	0.0788	−21.84	0.59	500	141	1.568	0.235	−17.0
A496	0.0329	−21.45	0.49	1114	228	2.304	0.346	−15.0
A514	0.0731	−22.20	0.40	920	183	2.102	0.315	−17.0
A629	0.1380	−22.80	0.44	1154	207	2.344	0.352	−18.0
A634	0.0265	−22.28	0.80	360	117	1.340	0.201	−16.5
A646	0.1303	−22.62	0.51	859	182	2.034	0.305	−18.0
A665	0.1816	−22.64	0.20	2068	272	3.101	0.465	−19.0
A671	0.0491	−22.32	0.35	1253	210	2.438	0.366	−16.0
A690	0.0788	−21.72	0.58	566	149	1.664	0.250	−17.0
A779	0.0229	−22.82	0.80	468	131	1.519	0.228	−16.0
A957	0.0437	−21.58	0.37	1037	191	2.226	0.334	−15.5
A999	0.0323	−22.22	1.01	357	117	1.334	0.200	−16.0
A1142	0.0349	−22.66	1.24	469	148	1.521	0.228	−15.0
A1213	0.0469	−23.06	0.59	966	184	2.151	0.323	−16.5
A1291	0.0530	−21.35	0.37	1146	202	2.336	0.350	−16.5
A1413	0.1427	−22.36	0.21	1737	249	2.852	0.428	−18.5
A1569	0.0784	−22.76	0.56	803	173	1.969	0.295	−17.0
A1650	0.0845	−21.88	0.26	1912	257	2.986	0.448	−17.0
A1656	0.0232	−22.04	0.31	2167	292	3.171	0.476	−14.50
A1775	0.0700	−21.59	0.38	1025	192	2.214	0.332	−16.5
A1795	0.0621	−21.50	0.28	1531	232	2.684	0.403	−16.5
A1913	0.0530	−22.54	0.40	980	187	2.166	0.325	−16.5
A1983	0.0430	−22.10	0.40	903	178	2.084	0.312	−16.0
A2022	0.0578	−22.91	0.56	1061	196	2.251	0.338	−17.0
A2029	0.0768	−22.07	0.20	1777	249	2.883	0.432	−17.0
A2152	0.0410	−21.92	0.40	801	169	1.967	0.295	−16.0
A2244	0.0997	−22.14	0.22	1674	243	2.802	0.420	−17.5
A2247	0.0385	−23.07	0.78	639	151	1.765	0.265	−16.5
A2255	0.0800	−22.60	0.21	2278	280	3.248	0.487	−17.0
A2256	0.0601	−22.51	0.21	2187	274	3.185	0.478	−16.5
A2271	0.0568	−21.46	0.51	669	157	1.804	0.270	−16.5
A2328	0.1470	−22.01	0.20	1935	263	3.004	0.450	−18.5
A2356	0.1161	−22.25	0.36	964	189	2.150	0.322	−18.0
A2384	0.0943	−22.38	0.29	1514	232	2.670	0.400	−17.5
A2399	0.0587	−22.16	0.54	676	157	1.813	0.272	−16.5
A2410	0.0806	−22.24	0.71	546	145	1.636	0.245	−17.0
A2415	0.0597	−21.74	0.44	940	184	2.123	0.318	−16.5
A2420	0.0838	−21.94	0.27	1239	210	2.425	0.364	−17.5
A2440	0.0904	−22.34	0.35	1050	196	2.240	0.336	−17.5
A2554	0.1108	−22.61	0.35	1221	211	2.408	0.361	−18.0
A2556	0.0865	−22.47	0.49	796	172	1.961	0.294	−17.0
A2593	0.0421	−22.25	0.40	1133	200	2.323	0.348	−16.0
A2597	0.0825	−21.56	0.58	696	163	1.839	0.276	−17.0
A2626	0.0573	−22.65	0.50	911	181	2.092	0.314	−16.5
A2634	0.0310	−22.30	0.32	1109	197	2.299	0.345	−16.5
A2657	0.0414	−22.44	0.51	723	162	1.872	0.281	−16.0
A2670	0.0761	−22.52	0.26	1783	249	2.888	0.433	−17.0

[a] The absolute R_c magnitude represents our adopted 100% completeness limit.

Barkhouse et al.

TABLE 2
COMPOSITE LUMINOSITY FUNCTION

Radius (r/r_{200})	M_1^* $(R_c$ mag$)$	χ_ν^2	M_2^* $(R_c$ mag$)$	α_2	χ_ν^2	No. of Clusters	$< B_{gc} >$ $(\mathrm{Mpc}^{1.8})$
0.0–0.2	$-22.26 \pm 0.06^{\mathrm{a}}$	0.64	$-17.43 \pm 0.07^{\mathrm{b}}$	-1.45 ± 0.10	0.94	42	$1066 \pm 397^{\mathrm{c}}$
0.2–0.4	-22.26 ± 0.07	1.04	-18.22 ± 0.05	-1.81 ± 0.04	4.50	39	1052 ± 378
0.4–0.6	-22.36 ± 0.10	0.58	-18.14 ± 0.05	-2.32 ± 0.05	3.24	28	961 ± 347
0.6–1.0	-22.38 ± 0.15	0.67	-18.39 ± 0.06	-2.46 ± 0.05	2.99	11	683 ± 205

[a] M_1^* is derived from a Schechter function fit to the bright-end of the LF with $\alpha_1 = -1.0$.
[b] M_2^* and α_2 are obtained from a Schechter function fit to the faint-end of the composite LF.
[c] The uncertainty is calculated from the dispersion of the mean.

TABLE 3
COMPOSITE RED SEQUENCE LUMINOSITY FUNCTION

Radius (r/r_{200})	M_1^* $(R_c$ mag$)$	χ_ν^2	M_2^* $(R_c$ mag$)$	α_2	χ_ν^2	No. of Clusters	$< B_{gc} >$ $(\mathrm{Mpc}^{1.8})$
0.0–0.2	$-22.28 \pm 0.07^{\mathrm{a}}$	0.69	$-16.95 \pm 0.58^{\mathrm{b}}$	-5.26 ± 15.51	3.96	42	$1066 \pm 397^{\mathrm{c}}$
0.2–0.4	-22.36 ± 0.08	1.29	-17.81 ± 0.22	-3.30 ± 0.64	1.45	39	1052 ± 378
0.4–0.6	-22.50 ± 0.12	0.72	-18.18 ± 0.24	-3.16 ± 0.51	1.16	28	961 ± 347
0.6–1.0	-22.61 ± 0.19	1.14	-18.60 ± 0.36	-2.83 ± 0.53	1.06	11	683 ± 205

[a] M_1^* is derived from a Schechter function fit to the bright-end of the LF with $\alpha_1 = -1.0$.
[b] M_2^* and α_2 are obtained from a Schechter function fit to the faint-end of the red sequence LF.
[c] The uncertainty is calculated from the dispersion of the mean.

Barkhouse et al.

TABLE 4
COMPOSITE BLUE LUMINOSITY FUNCTION

Radius (r/r_{200})	M_1^* (R_c mag)	χ_ν^2	M_2^* (R_c mag)	α_2	χ_ν^2	No. of Clusters	$< B_{gc} >$ (Mpc$^{1.8}$)
0.0–0.2	$-21.96 \pm 0.26^{\text{a}}$	0.28	$-19.30 \pm 0.10^{\text{b}}$	-1.62 ± 0.05	0.61	42	$1066 \pm 397^{\text{c}}$
0.2–0.4	-21.84 ± 0.17	0.36	-19.28 ± 0.09	-1.64 ± 0.05	0.93	39	1052 ± 378
0.4–0.6	-21.81 ± 0.21	1.21	-19.01 ± 0.12	-1.69 ± 0.09	1.05	28	961 ± 347
0.6–1.0	-21.87 ± 0.27	0.74	-18.79 ± 0.12	-1.82 ± 0.10	0.61	11	683 ± 205

[a] M_1^* is derived from a Schechter function fit to the bright-end of the LF with $\alpha_1 = -1.0$.
[b] M_2^* and α_2 are obtained from a Schechter function fit to the faint-end of the blue galaxy LF.
[c] The uncertainty is calculated from the dispersion of the mean.
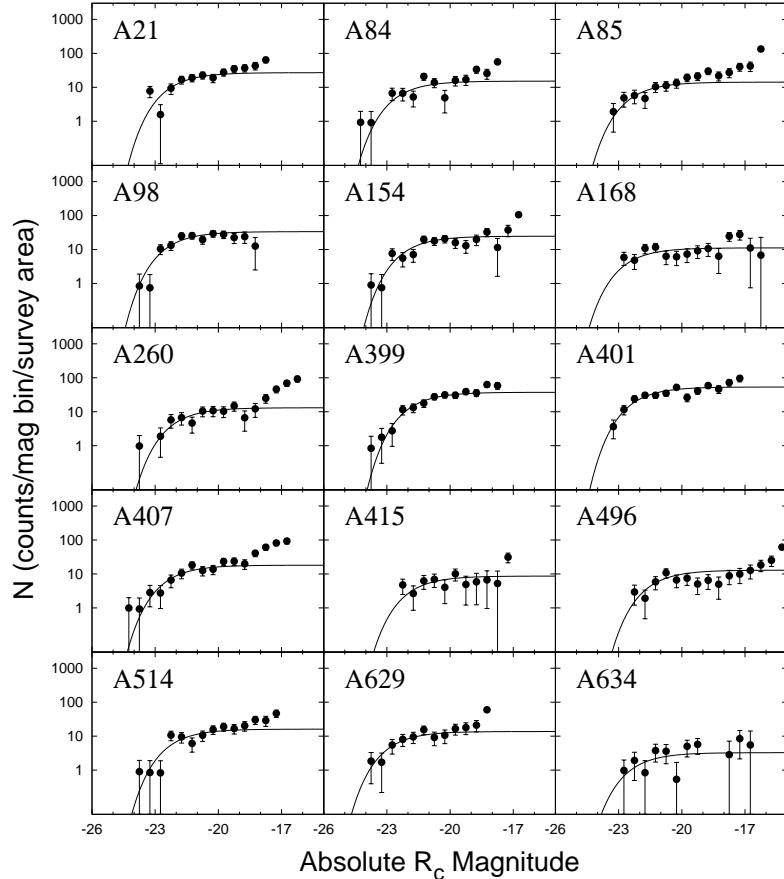
FIG. 1A.— Solid points depict the R_c-band luminosity function for 57 Abell clusters. The solid line represents the best-fit Schechter function with a fixed faint-end slope of $\alpha = -1$. The galaxy counts are measured from within a cluster-centric radius of $(r/r_{200}) = 0.4$, except for A496 and A1142 due to the lack of adequate radial coverage. The brightest cluster galaxy has been omitted from each LF.
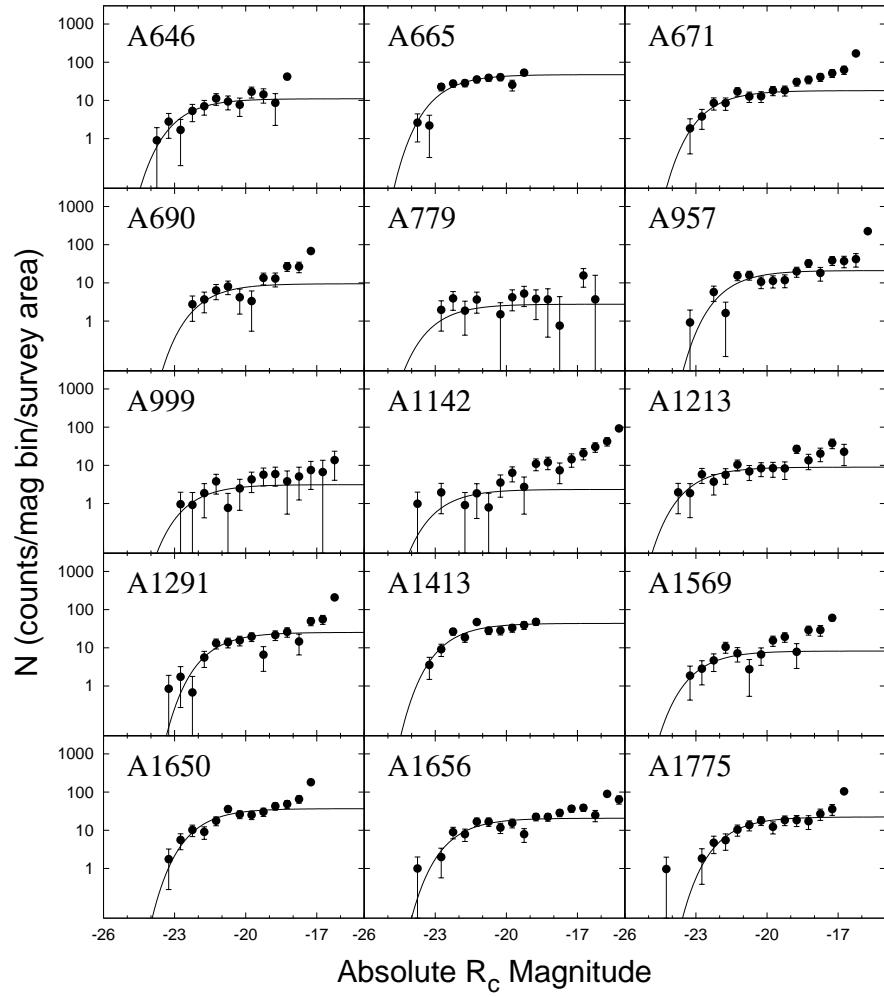
FIG. 1B.— Continued
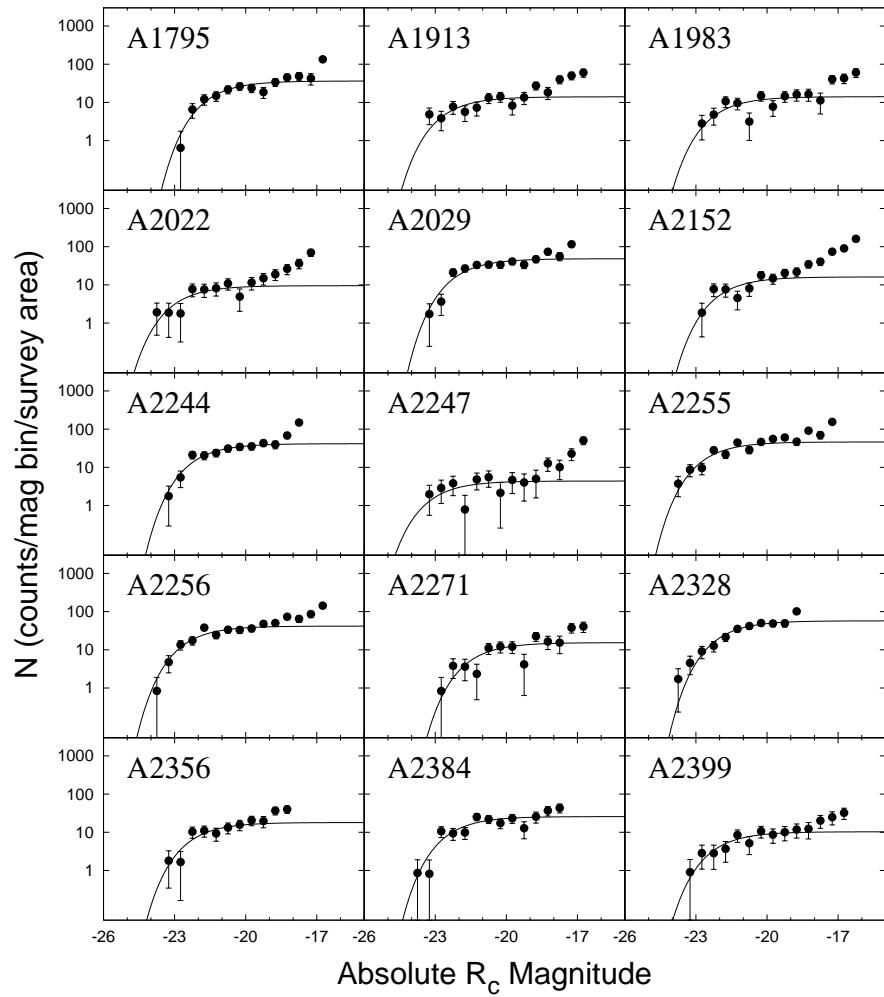
Fig. 1c.— Continued
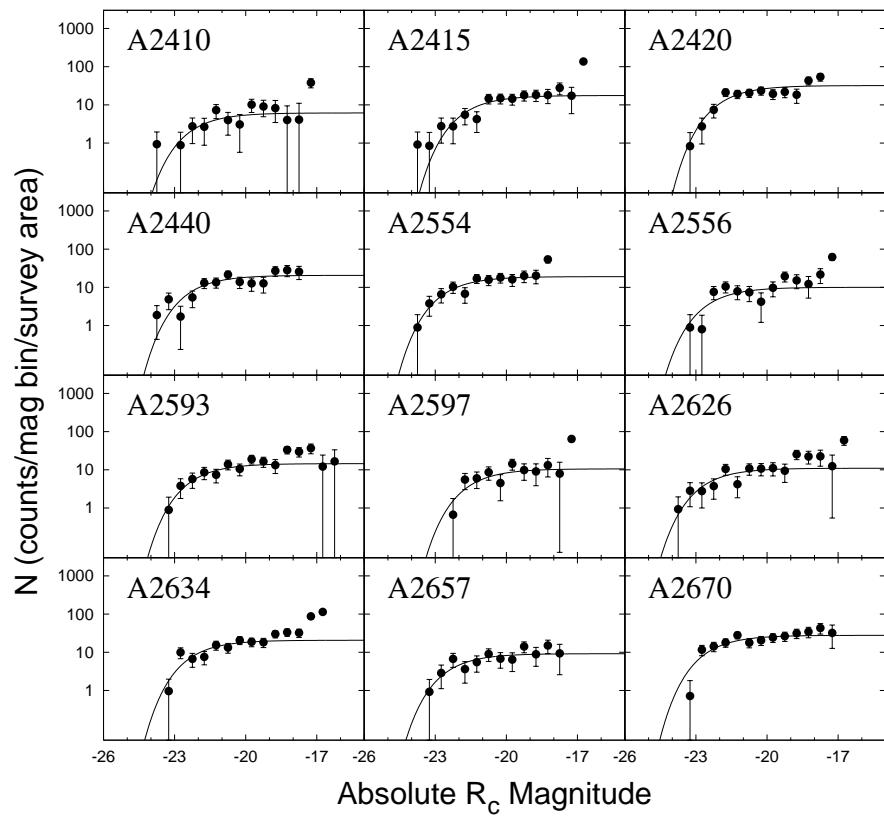
FIG. 1D.— Continued
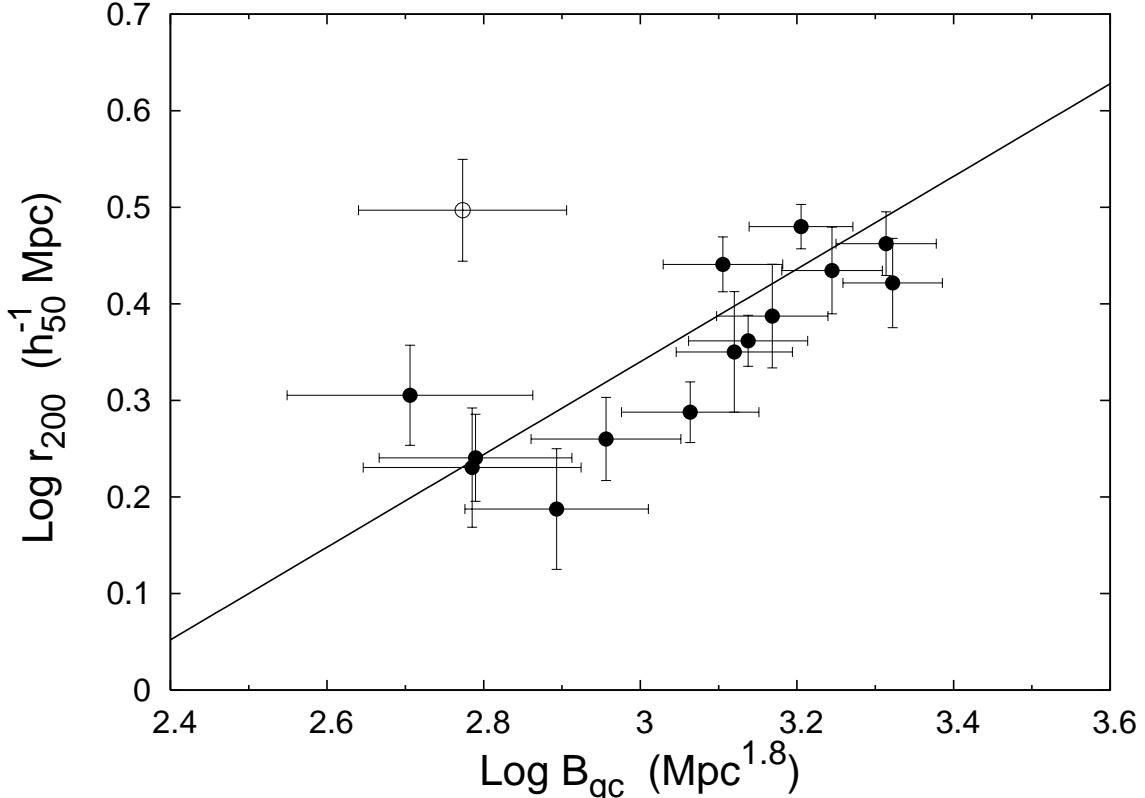
FIG. 2.— Logarithmic correlation between r_{200} and B_{gc} for 15 clusters from the CNOC1 cluster sample. The solid line is a fit using the BCES estimator to the 14 clusters depicted by the solid circles. The open circle represents the outlier cluster MS 1455+22, which was not used in the fitting process. The rms scatter in the derived values of r_{200} is on the order of 15%.
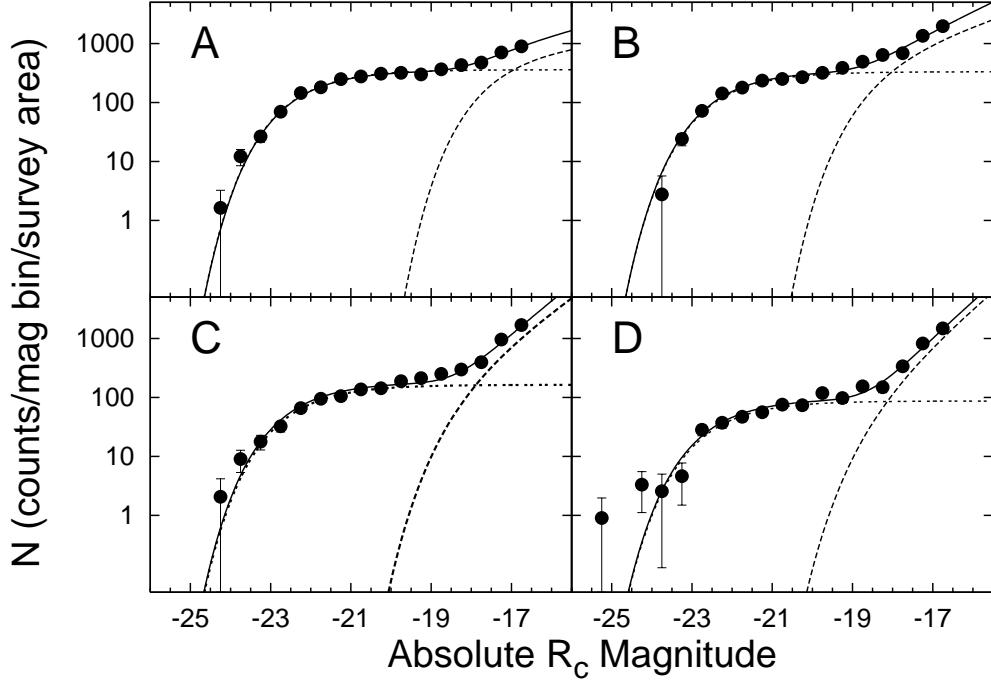
FIG. 3.— Composite total R_c-band luminosity function for four cluster-centric annuli: A) $(r/r_{200}) \leq 0.2$, B) $0.2 \leq (r/r_{200}) \leq 0.4$, C) $0.4 \leq (r/r_{200}) \leq 0.6$, and D) $0.6 \leq (r/r_{200}) \leq 1.0$. The short dashed line represents a Schechter function fit to bright-end with a fixed faint-end slope, $\alpha = -1$. The solid circles depict the combined net galaxy counts for all contributing clusters. The long dashed line is a Schechter function fit to the faint-end, while the solid line is the sum of the two Schechter functions.
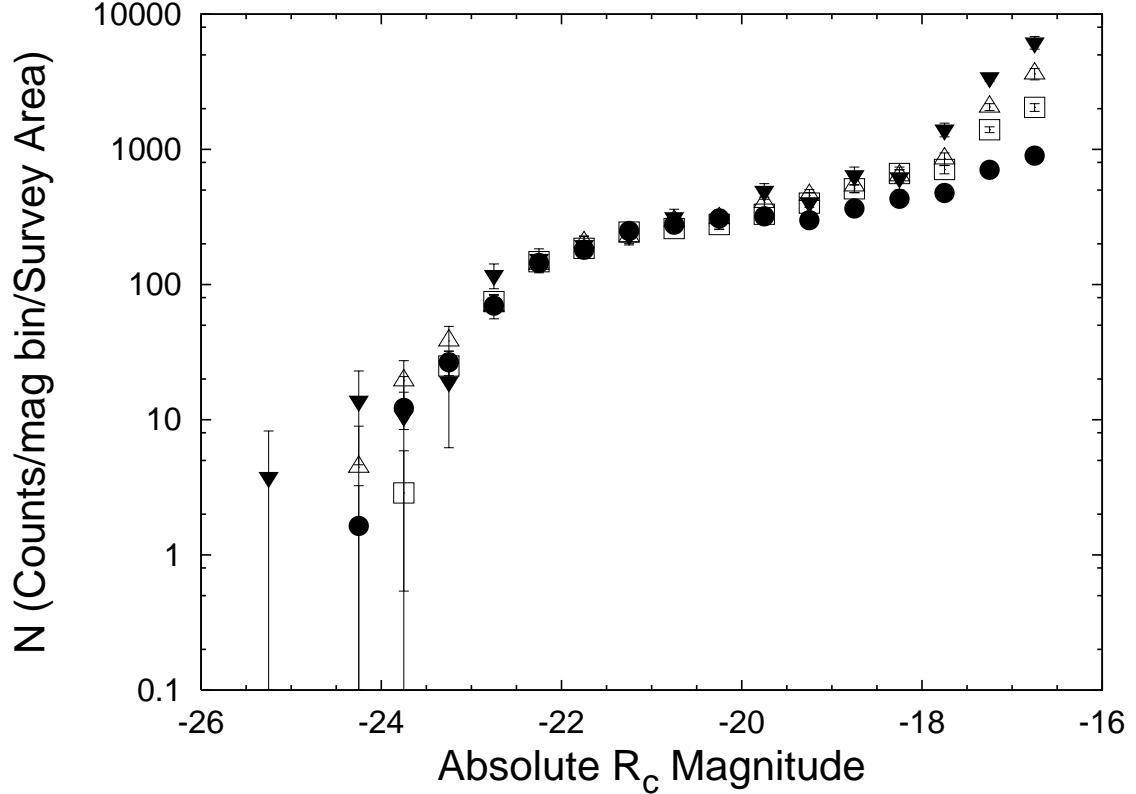
FIG. 4.— Superposition of the total composite LF measured for four cluster-centric radial bins. The outer three LFs have been scaled to match the inner-most LF in the $-22 \leq M_{R_c} \leq -21$ magnitude range. The plot symbols depict the following: solid circles — the net galaxy counts in the $(r/r_{200}) \leq 0.2$ annulus; open squares — the counts in the $0.2 \leq (r/r_{200}) \leq 0.4$ annulus; open triangles — the galaxy counts in the $0.4 \leq (r/r_{200}) \leq 0.6$ radial bin; and the solid triangles — the $0.6 \leq (r/r_{200}) \leq 1.0$ annulus.
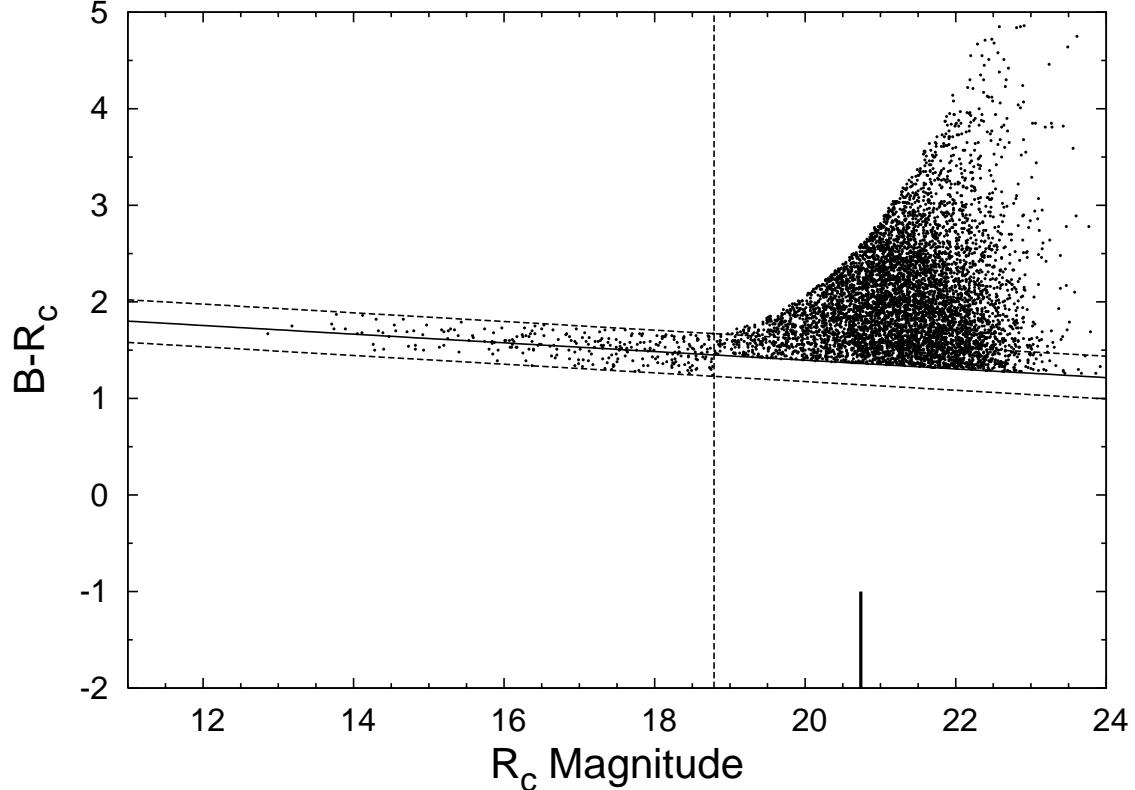
FIG. 5.— Color-magnitude diagram for A260, depicting the region where red sequence galaxies were selected. For galaxies brighter than $R_c = 18.8$ (dashed vertical line), red sequence galaxies are designated as those within ± 0.22 mag ($\pm 3\sigma$) of the cluster red sequence relation (nearly horizontal solid line). Galaxies fainter than $R_c = 18.8$ are selected if they lie within the region $2.5\sigma_{B-R_c}$ redward of the red sequence and brighter than the magnitude completeness limit (solid short vertical line).
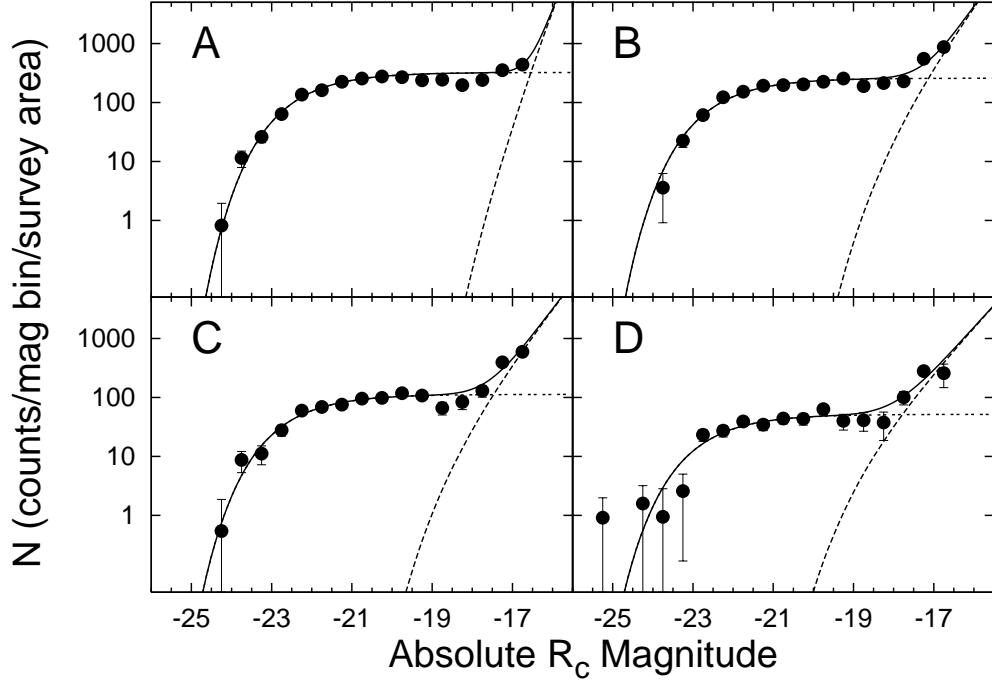
FIG. 6.— Composite red sequence R_c-band LF for four cluster-centric annuli: A) $(r/r_{200}) \leq 0.2$, B) $0.2 \leq (r/r_{200}) \leq 0.4$, C) $0.4 \leq (r/r_{200}) \leq 0.6$, and D) $0.6 \leq (r/r_{200}) \leq 1.0$. The short dashed line represents a Schechter function fit to bright-end with a fixed faint-end slope, $\alpha = -1$. The solid circles depict the combined net galaxy counts for all contributing clusters in each annulus. The long dashed line is a Schechter function fit to the faint-end, while the solid line is the sum of the two Schechter functions.
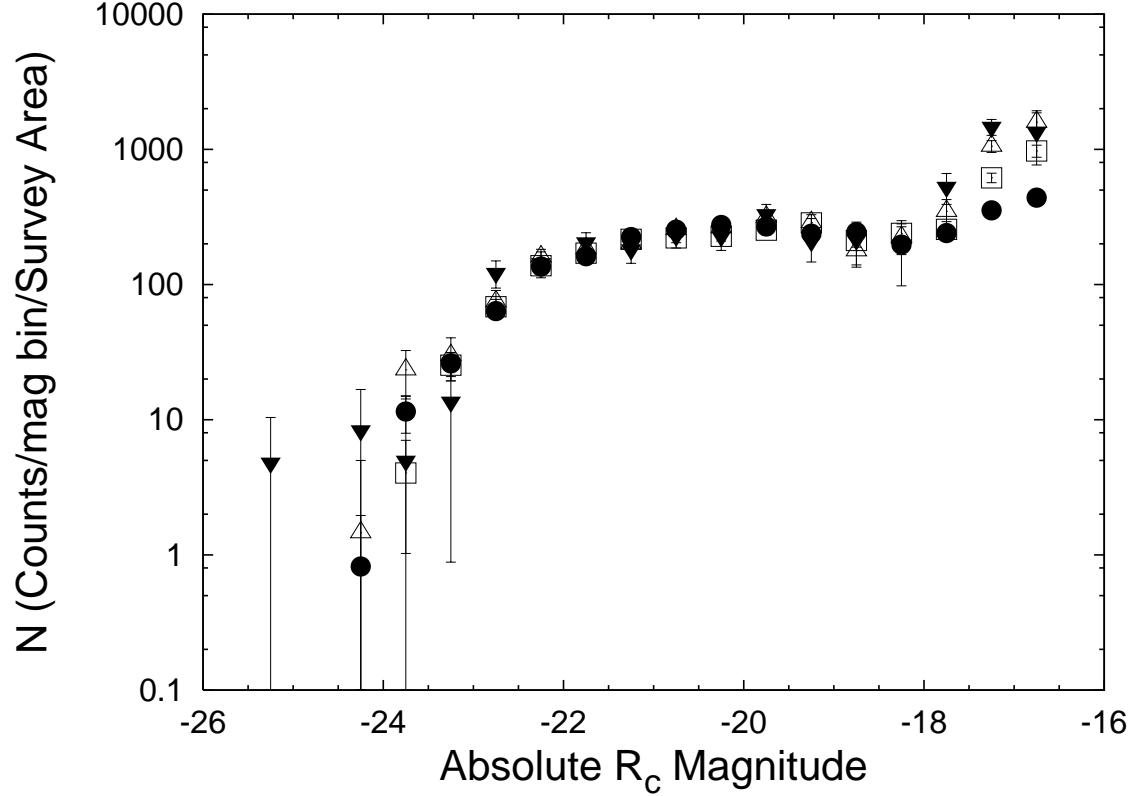
FIG. 7.— Superposition of the red sequence composite LF measured for four cluster-centric radial bins. The outer three LFs have been scaled to match the inner-most LF in the $-22 \leq M_{R_c} \leq -21$ magnitude range. Plot symbols are equivalent to those defined in Figure 4.
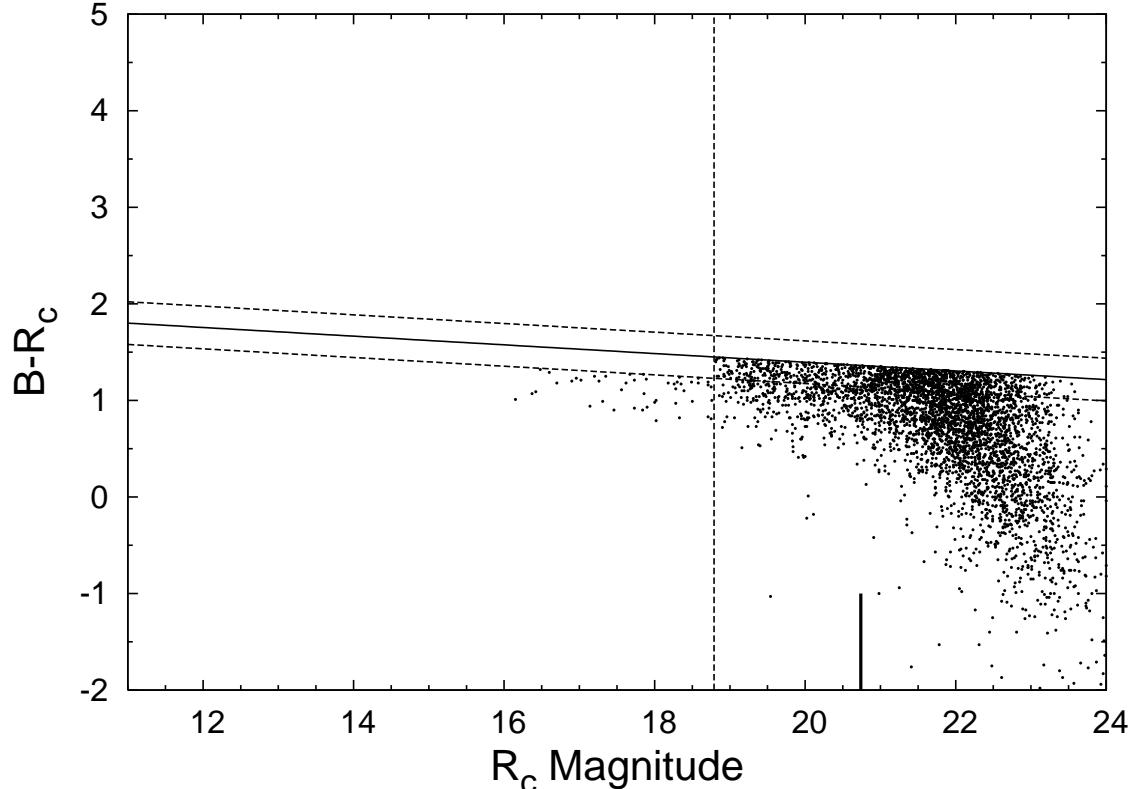
FIG. 8.— Color-magnitude diagram for A260, depicting the region used to select the blue cluster galaxy population. For galaxies brighter than $R_c = 18.8$ (dashed vertical line), blue galaxies are designed as those with $B - R_c$ color bluer than the lower envelope used to select the red sequence galaxies. Galaxies fainter than $R_c = 18.8$ and brighter than the completeness limit ($R_c = 20.7$, short vertical line), are selected if they are located in the region bluer than the lower envelope (blueward of the CMR) defining the boundary of the region used to select red sequence galaxies.
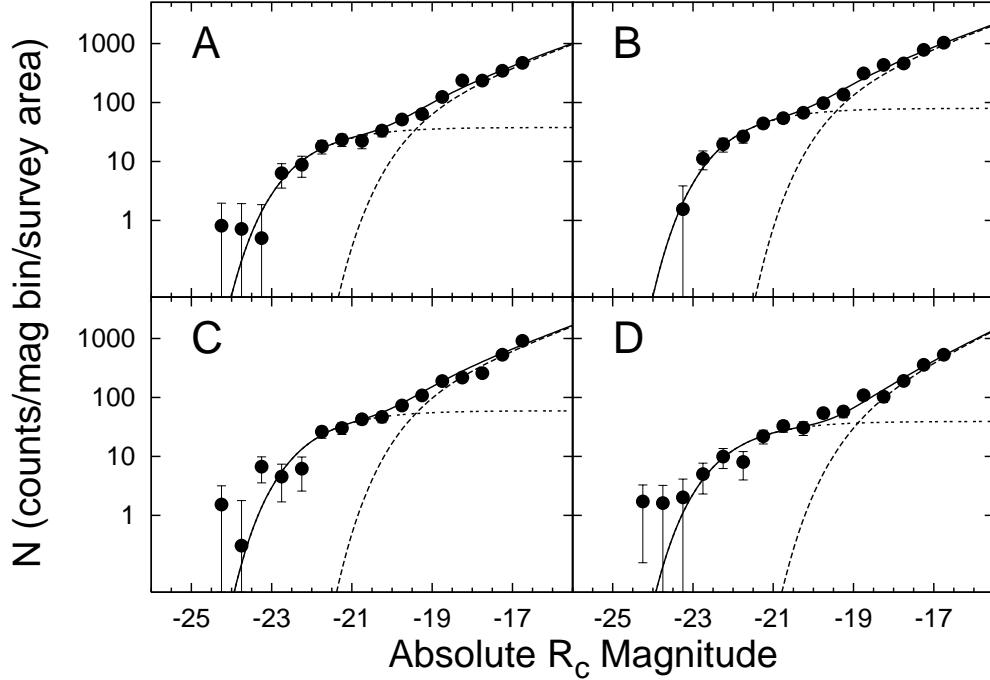
FIG. 9.— Composite blue galaxy R_c-band LF for four cluster-centric annuli: A) $(r/r_{200}) \leq 0.2$, B) $0.2 \leq (r/r_{200}) \leq 0.4$, C) $0.4 \leq (r/r_{200}) \leq 0.6$, and D) $0.6 \leq (r/r_{200}) \leq 1.0$. The short dashed line represents a Schechter function fit to bright-end with a fixed faint-end slope, $\alpha = -1$. The solid circles depict the combined net galaxy counts for all contributing clusters in each annulus. The long dashed line is a Schechter function fit to the faint-end, while the solid line is the sum of the two Schechter functions.
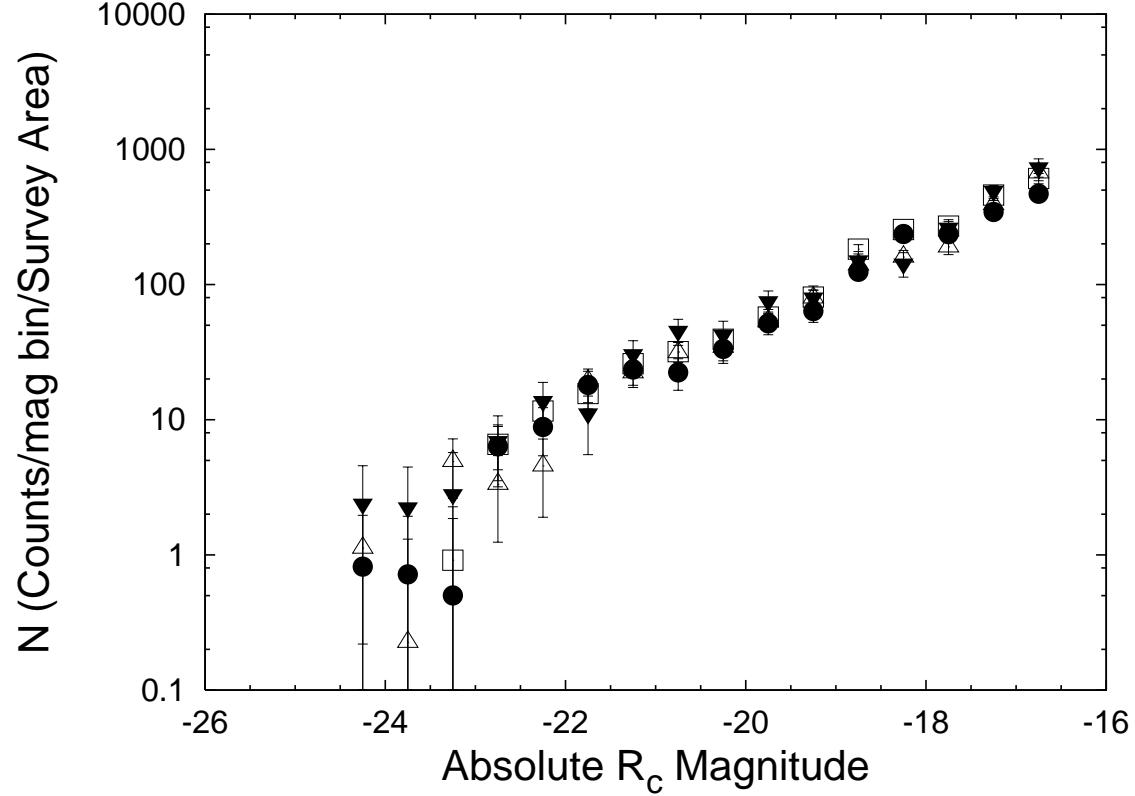
Fig. 10.— Superimposed composite blue galaxy LFs measured for four cluster-centric radial bins. The outer three LFs have been scaled to match the inner-most LF in the $-22 \leq M_{R_c} \leq -21$ magnitude range. Plot symbols are equivalent to those defined in Figure 4.
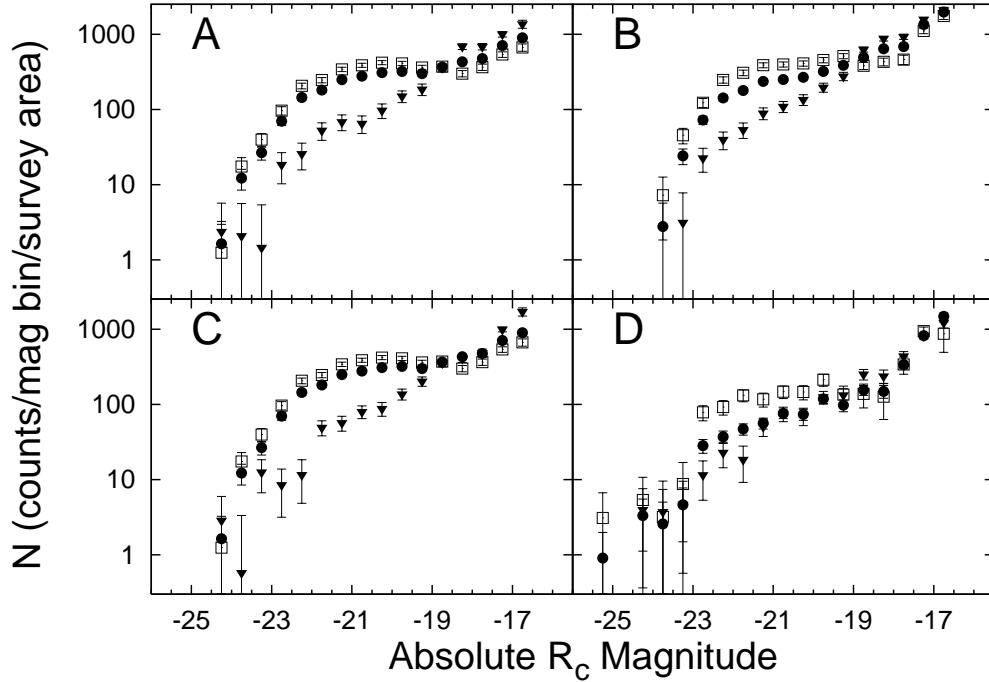
Fig. 11.— Composite LF for the total, red sequence, and blue galaxy populations for four radial bins depicted in previous figures (e.g., see Figure 9). The red sequence and blue LFs (represented by open squares and solid triangles, respectively) have been scaled to have the same net galaxy counts as the total LF (solid circles) in the $-24.0 \leq M_{R_c} \leq -16.5$ magnitude range.
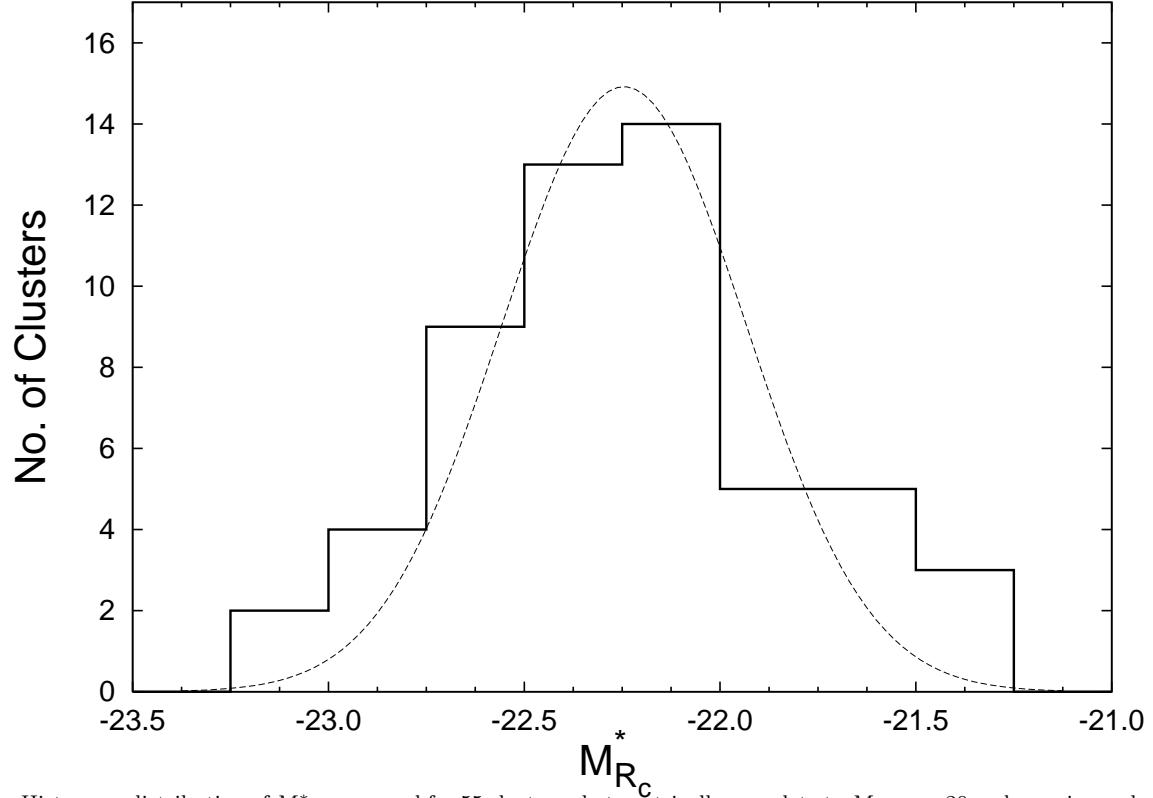
FIG. 12.— Histogram distribution of $M_{R_c}^*$ measured for 55 clusters photometrically complete to $M_{R_c} = -20$ and covering a cluster-centric radius of $(r/r_{200}) = 0.4$. The distribution of $M_{R_c}^*$ is approximately Gaussian with $\langle M_{R_c}^* \rangle = -22.24 \pm 0.06$ and a dispersion of $\sigma = 0.31$ mag (dashed line).

Barkhouse et al.
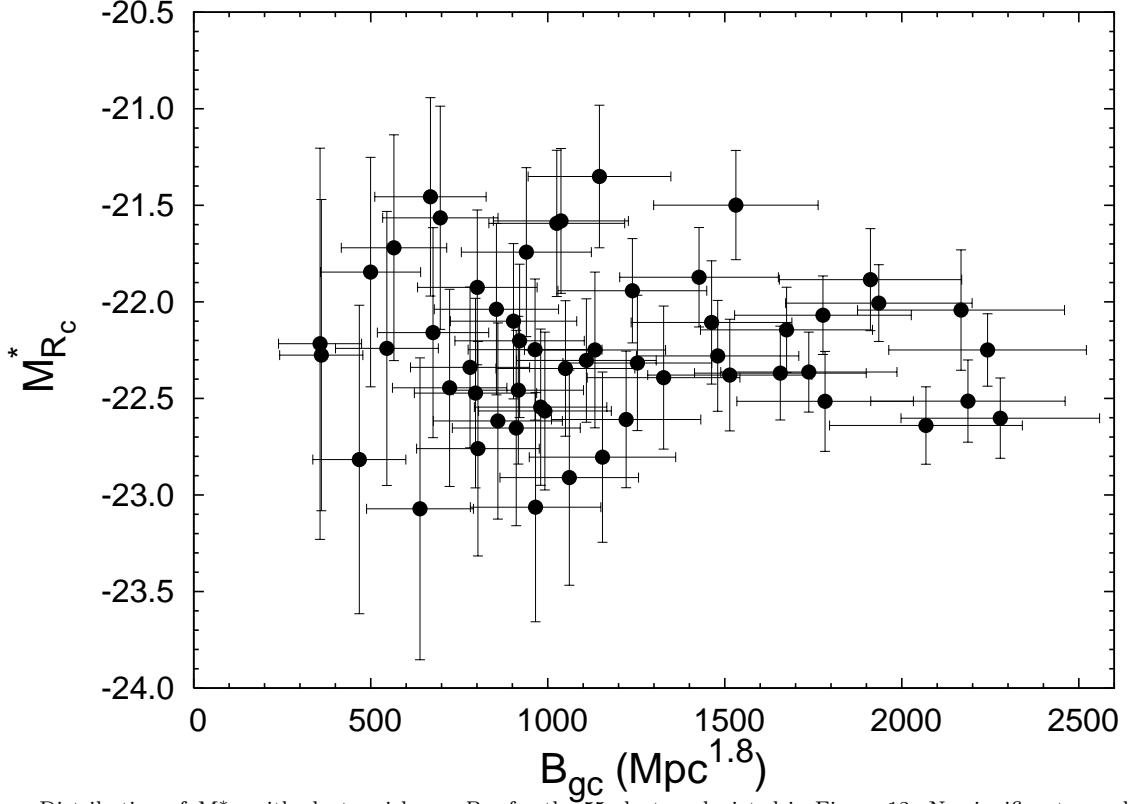
FIG. 13.— Distribution of $M^*_{R_c}$ with cluster richness B_{gc} for the 55 clusters depicted in Figure 12. No significant correlation between $M^*_{R_c}$ and B_{gc} was found for our sample.
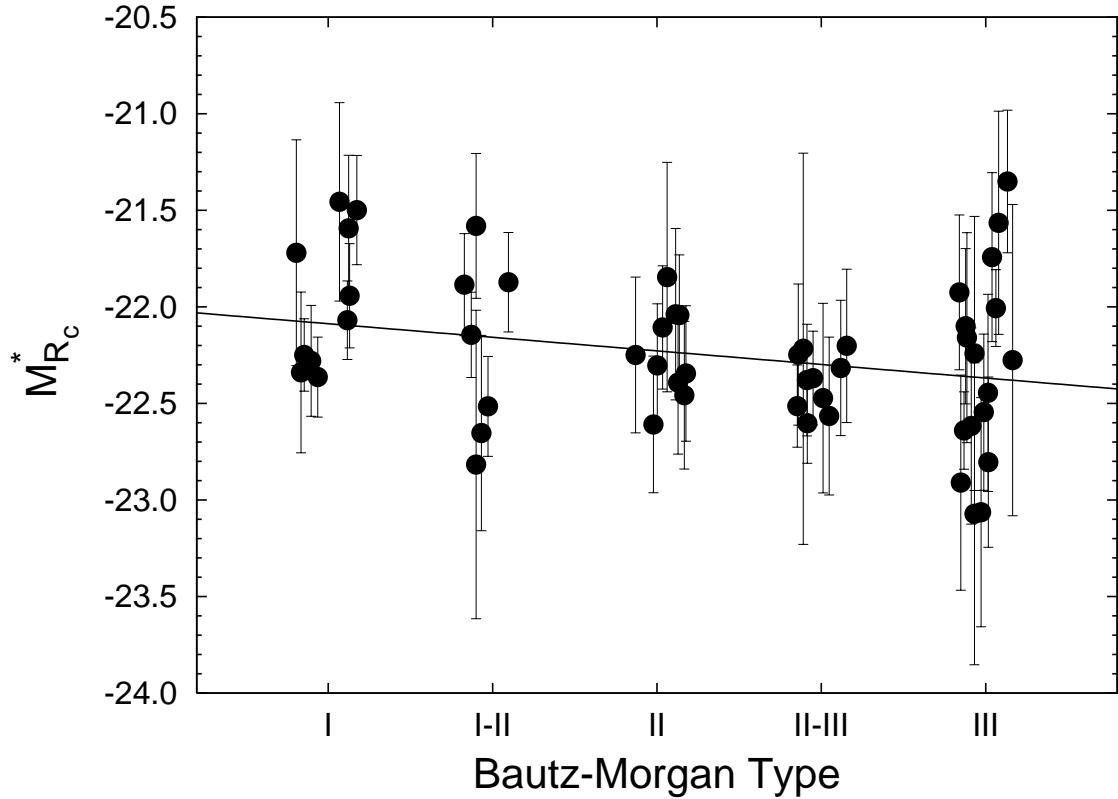
FIG. 14.— $M^*_{R_c}$ as a function of BM-type for 54 of the 55 clusters depicted in Figure 13. The solid line represents a least-squares fit to the data and indicates that $M^*_{R_c}$ brightens for later BM-type. A Spearman rank-order correlation coefficient test yields that the two measurements are correlated at the 96% significance level.
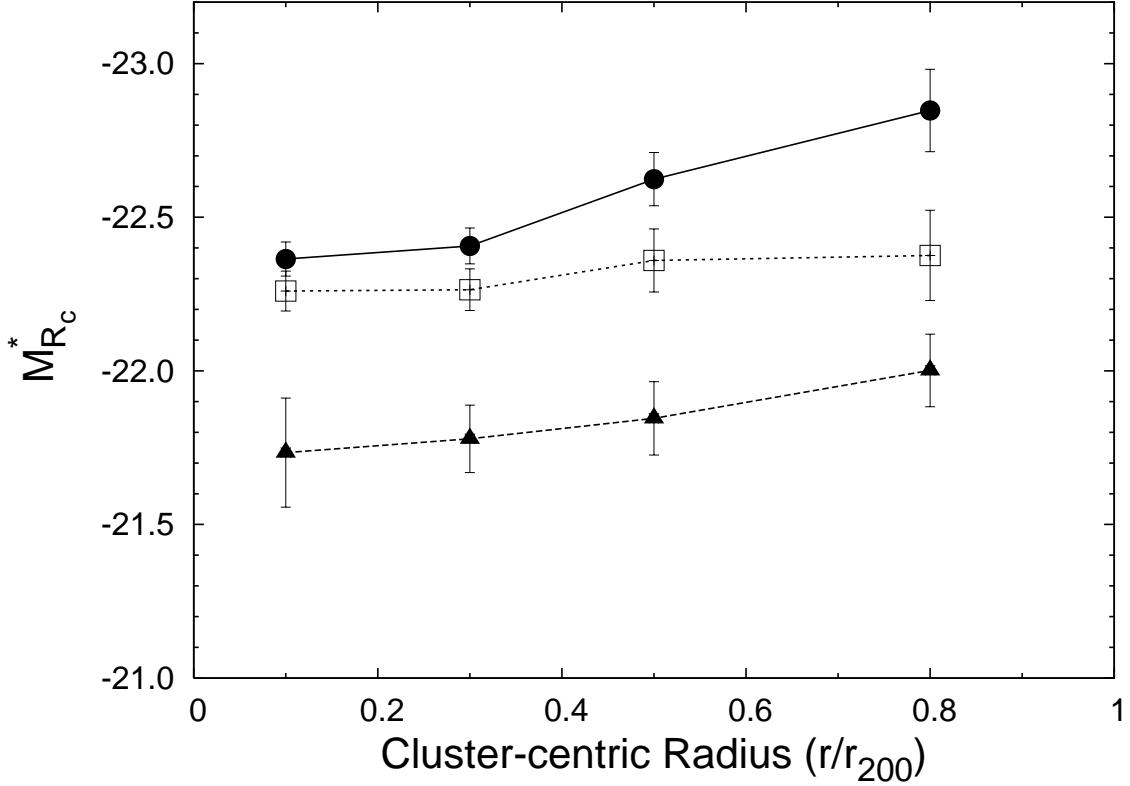
FIG. 15.— Variation in $M^*_{R_c}$ with cluster-centric radius for the total (open squares), red sequence (solid circles), and blue galaxy populations (solid triangles). $M^*_{R_c}$ is measured for a composite sample of 57 clusters complete to $M_{R_c} = -20$. The red sequence and blue galaxy samples exhibit a trend in which $M^*_{R_c}$ becomes brighter with increasing cluster-centric radius.
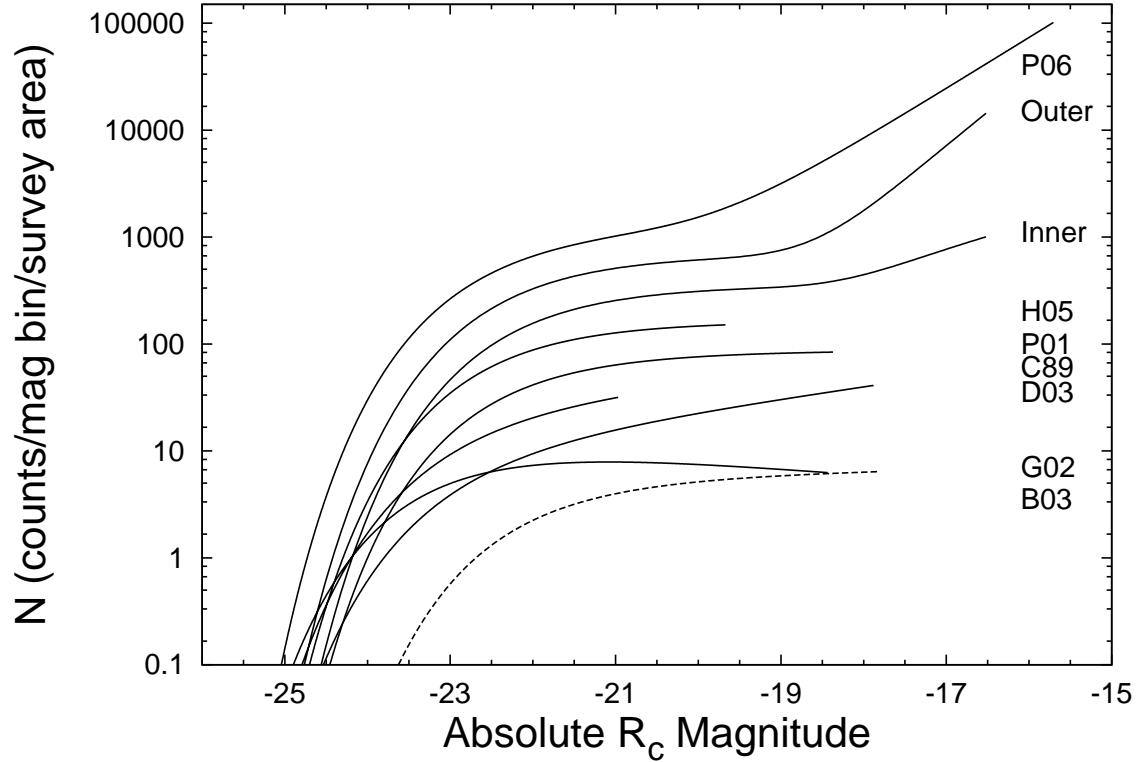
FIG. 16.— Comparison of cluster LFs with published sources: P06 – Popesso et al. 2006, Outer — this paper, composite total LF for $0.6 \leq (r/r_{200}) \leq 1.0$, Inner – this paper, composite total LF for $(r/r_{200}) \leq 0.2$, H05 – Hansen et al. 2005, P01 – Piranomonte et al. 2001, C89 – Colless 1989, D03 – De Propris et al. 2003, G02 – Goto et al. 2002, and B03 – Blanton et al. 2003 (SDSS field LF; dashed line). The LFs have been scaled by 0.3 dex relative to each other for comparison purposes.
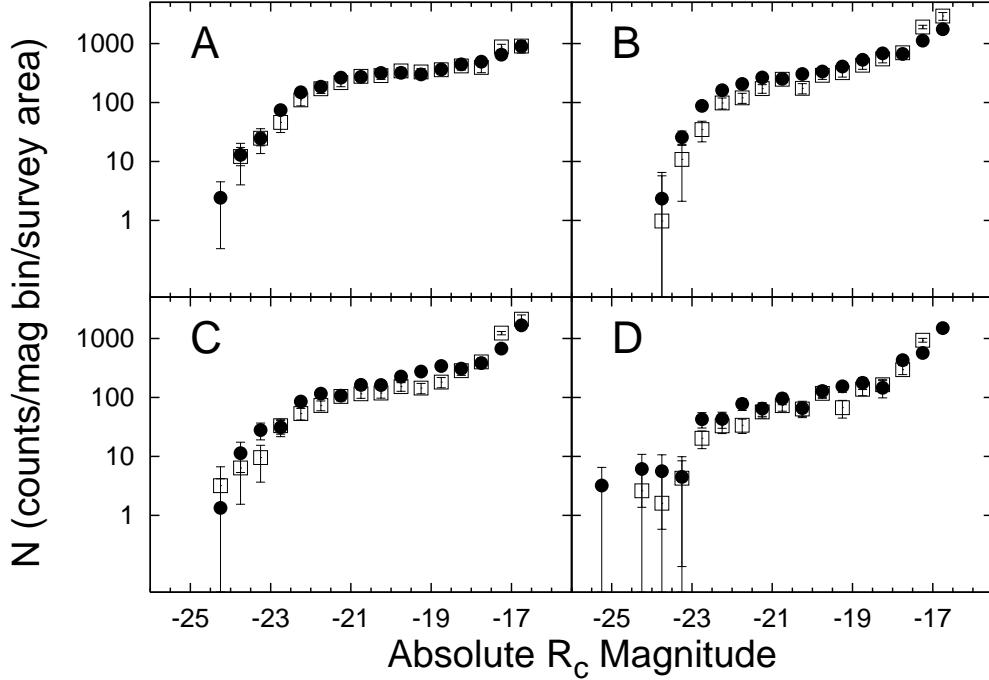
FIG. 17.— Composite total R_c-band LF for two groups of clusters containing ≤ 10 redshift-confirmed galaxies (open squares) and ≥ 25 redshift-confirmed galaxies (solid circles). The LFs have been scaled to match the total composite LF in the $-24 \leq M_{R_c} \leq -17$ magnitude range. The four radial bins are equivalent to those used in Figure 3.
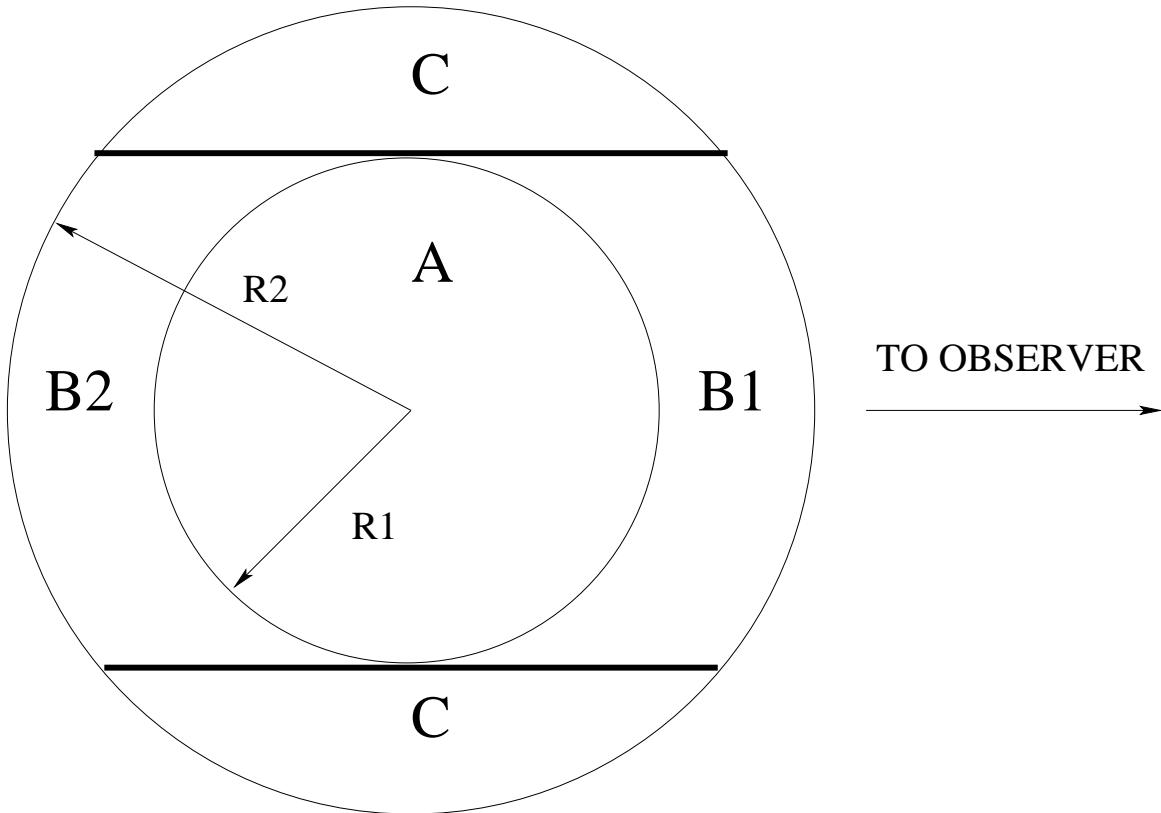
FIG. 18.— Schematic diagram illustrating the geometry used to convert the projected LF to the deprojected LF. The projected central LF from region A will be contaminated by projected galaxies from regions B1 and B2 that lie in the cluster outskirts. The LF in region C can be utilized to deproject the central LF and thus minimize the influence of the contaminating galaxies.
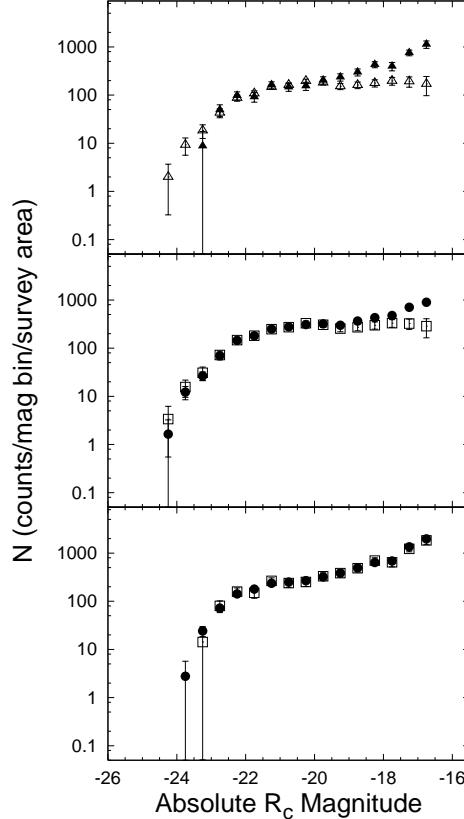
FIG. 19.— **Top Panel:** Deprojected total composite LFs are compared for the inner-most radial bin $(r/r_{200}) \leq 0.2$ (open triangles) with the $0.2 \leq (r/r_{200}) \leq 0.4$ radial bin (solid triangles). The outer deprojected LF has been scaled to match the inner LF in the $-22 \leq M_{R_c} \leq -21$ magnitude range. **Middle Panel:** The deprojected total composite LF (open squares) is compared to the projected LF (solid circles) for the $(r/r_{200}) \leq 0.2$ annulus. The deprojected LF has been scaled to match the projected LF in the $-22 \leq M_{R_c} \leq -21$ magnitude interval. **Bottom Panel:** The deprojected total composite LF (open squares) is compared to the projected LF (solid circles) for the $0.2 \leq (r/r_{200}) \leq 0.4$ annulus. The deprojected LF has been scaled to match the projected LF in the $-22 \leq M_{R_c} \leq -21$ magnitude range.
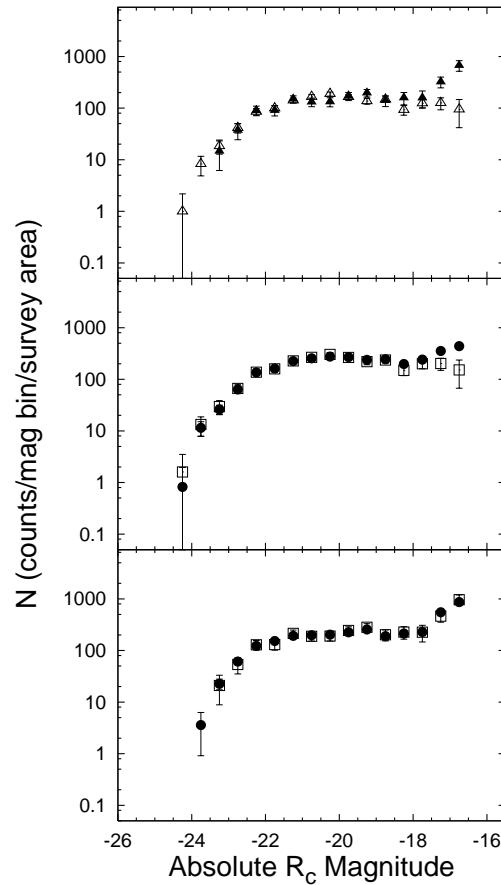
FIG. 20.— Same as Figure 19, but for the red sequence composite LF.
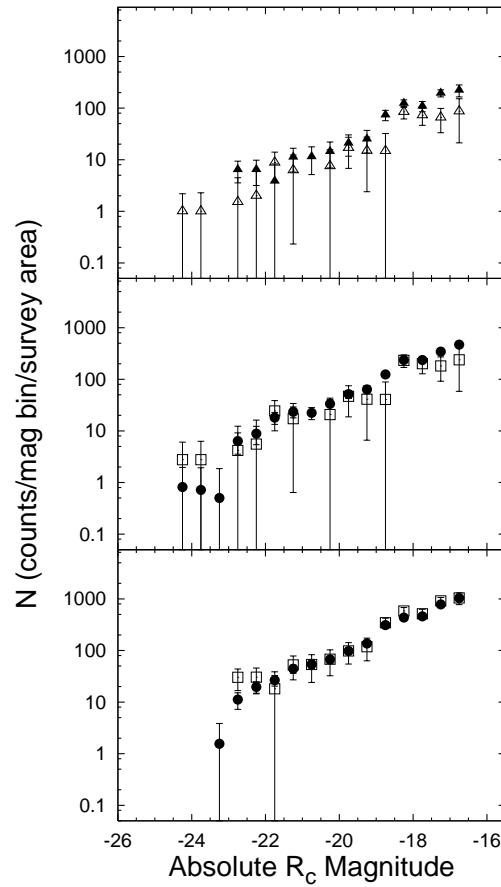
Fig. 21.— Same as Figure 19, but for the blue composite LF.
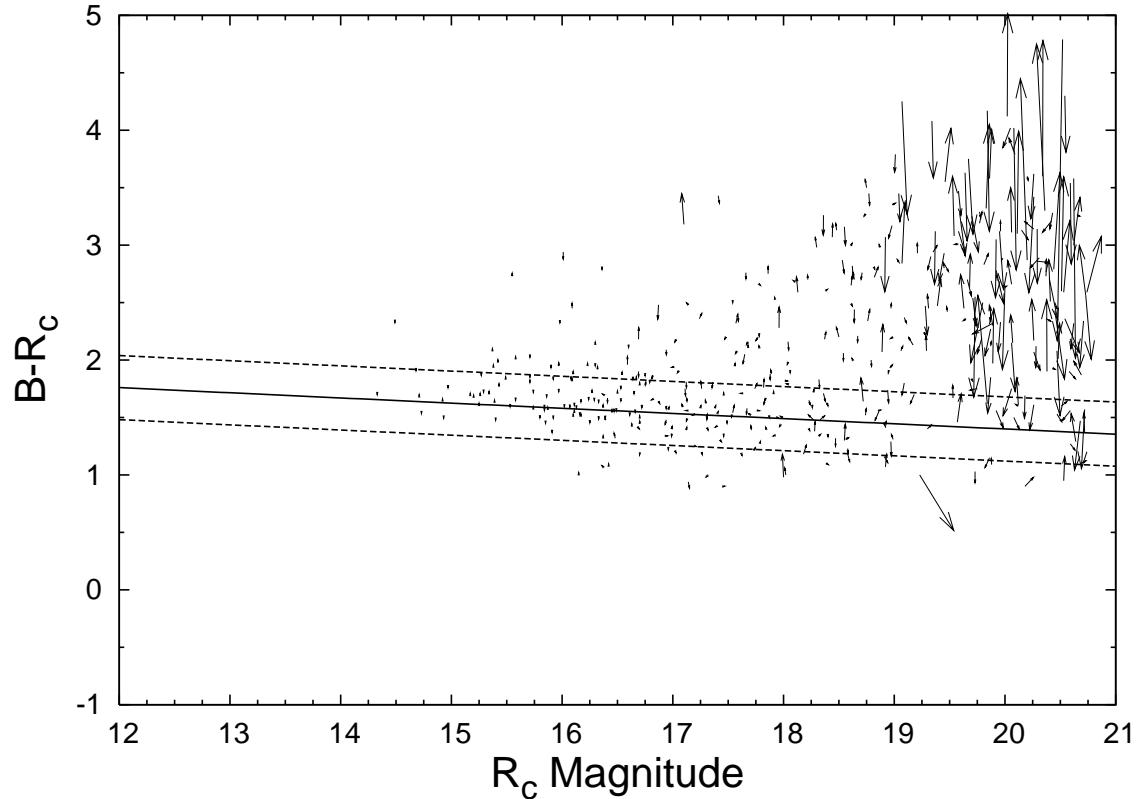
FIG. 22.— Vector-style color-magnitude diagram for A260. The vectors define the relative change in $B - R_c$ color and R_c-mag for the position of the observed galaxies to the location of the simulated galaxies. The cluster CMR is depicted by the horizontal solid line and the $\pm 3\sigma$ limit by the dashed line. For clarity, only a fraction of the cluster galaxies brighter than the magnitude completeness limit for this cluster are displayed.
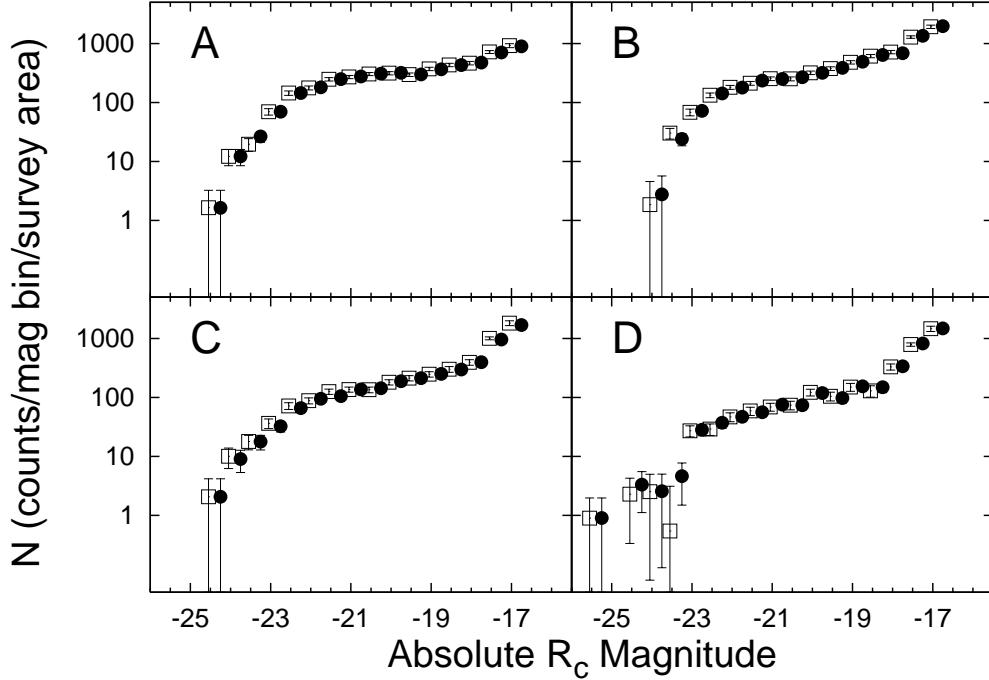
Fig. 23.— Composite total observed LF (solid circles) is compared to the simulated LF (open squares) for the four radial bins used previously: A) $(r/r_{200}) \leq 0.2$, B) $0.2 \leq (r/r_{200}) \leq 0.4$, C) $0.4 \leq (r/r_{200}) \leq 0.6$, and D) $0.6 \leq (r/r_{200}) \leq 1.0$. The simulated LF is constructed by randomly changing r_{200} by $\pm15\%$. The simulated LFs have been offset by 0.3 mag in order to assist the comparison.
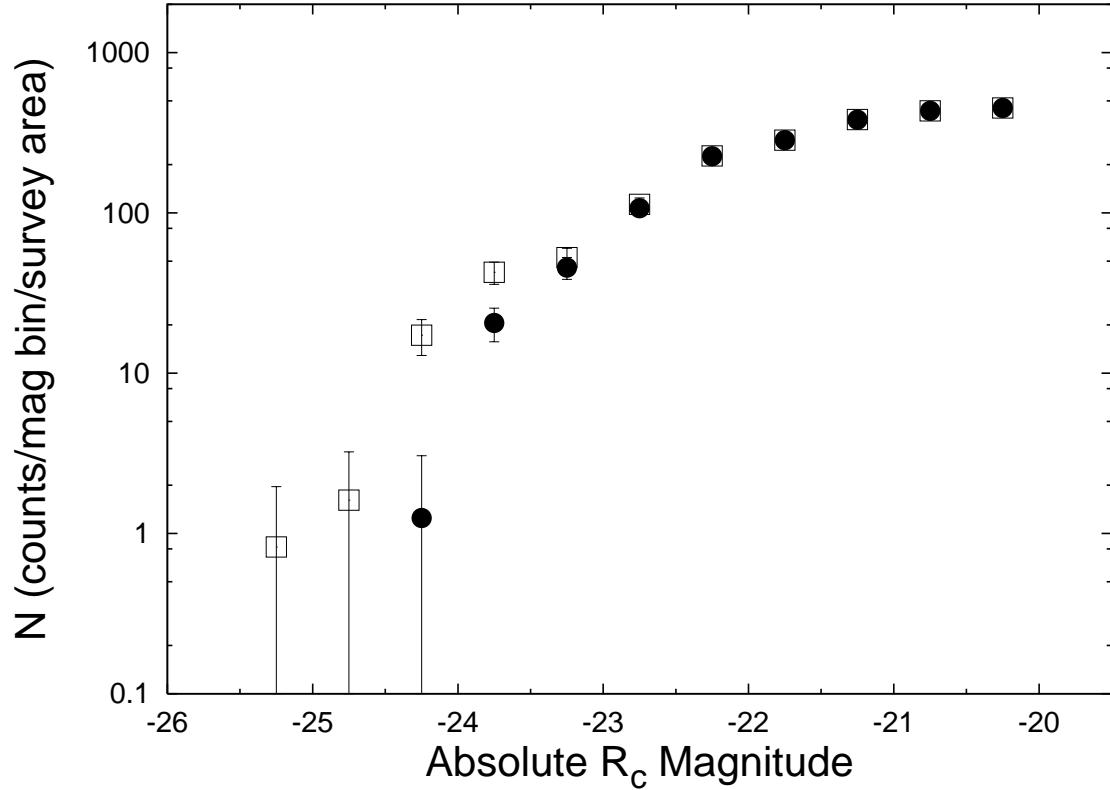
FIG. 24.— Comparison of the total composite LF for 57 clusters that are photometrically complete to $M_{R_c} = -20$ and cover the $(r/r_{200}) \leq 0.2$ annulus. The solid points represent the LF comprised by excluding the BCGs from the net galaxy counts. The inclusion of the BCGs in the LF is depicted by the open squares.